ORNL/TM-2013/217

Light Water Reactor Sustainability Program

Analysis of Deformation Mode Changes in Irradiated Materials using Bend Tests and Finite Element Modeling

June 2013

U.S. Department of Energy

Office of Nuclear Energy

ORNL/TM-2013/217

Analysis of Deformation Mode Changes in Irradiated Materials using Bend Tests and Finite Element Modeling

M. N. Gussev, J. T. Busby

Oak Ridge National Laboratory

June 2013

Prepared for the
U.S. Department of Energy
Office of Nuclear Energy

Light Water Reactor Sustainability Program

Analysis of Deformation Mode Changes in Irradiated Materials using Bend Tests and Finite Element Modeling

ORNL/TM-2013/217

June 2013

Approved by:

Jeremy T. Busby	6/12/2013
Name Materials Aging and Degradation Pathway Lead	Date
Name Title [optional]	Date
Name Title [optional]	Date
Name Title [optional]	Date

Abstract

To overcome limitations caused by irradiated materials availability, a new miniature bend test assembly was designed and produced. The assembly allows one to conduct 3- and 4-point bend tests with various span distances and provides an ability to conduct in-situ optic measurements and microstructure observations. A set of materials including 304 and 316 stainless steels and model alloys irradiated up to 47 dpa was tested using the assembly. Bend test method coupled with finite element modeling allows one to define mechanical properties of material, investigate its deformation behavior, and define stress and strain distribution in the deformed specimen which is important for following structure investigation.

Using this assembly, phase and structure transformations (martensite formation and twinning, respectively) were investigated in irradiated steels and alloys; new results on morphology of twins and martensite in irradiated materials were obtained. Deformation modes, dynamics of deformation localization, and dislocation channeling were studied in-situ. Some interesting data on dislocation channels evolutions were obtained; one of the most interesting results is channels spatial organization. Also, a specific new form of deformation martensite associated with dislocation channels was found and analyzed.

.

Analysis of deformation mode changes in irradiated materials using bend tests and finite element modeling

M. N. Gussev, J. T. Busby

Contents

1. Introduction

Because there are limited facilities available for irradiating materials and alloys and because high dose irradiations are expensive, the amount of irradiated material very often is limited, and it is not always possible to conduct conventional tensile test. Also, due to high level of radioactivity, it could be beneficial to limit the dimensions of specimen and use small-scale specimens and special test methods. Given the limits on materials and safety concerns, it is beneficial to examine new testing techniques. Three- or 4-bend test is one of the available options. Bend test allow one to define yield stress, also as evaluate estimate plastic hardening behavior. Coupled with finite element analysis, bend test provides a way to getting full true strain – true stress curve. Further, these tests often allow for smaller or irregular materials to be tested.

Comparing to conventional tensile test, bending does not provide uniform strain and stress distribution in the deformed volume even at small plastic strains; however, under some circumstances this could be considered an advantage. In particular, for one single specimen of some unique alloy, a bend test allows one to obtain a deformed object with a wide range of deformation microstructures.

In the present work, new miniature multifunctional bend test assembly was designed and produced. Using this assembly, 3- and 4-point bend tests were conducted with a set of unique model alloys irradiated to 4.4-10.2 dpa; phase and structure transformations and deformation modes were studied using in-situ optic microscopy, ESM-EBSD, FEA, magnetometry and other research methods.

2. Bend test experiments

2.1. Bend assembly design

To conduct deformation bend experiments, new experimental assembly was designed and manufactured. The assembly (see Fig.1) consists of the matrix of complex shape and a loading punch which moves along two guide rods. All parts were made of 17-4 HP steel. The maximum allowed load is ~4 kN, and the assembly passed ~3 kN load test without any deformation or damage. Tungsten carbide was selected as a material for supporting and loading rods. The diameter of rods may vary from 0.5 to 1. 5 mm; in the present work rods of 1.23 mm diameter were used.

The assembly was designed to allow one conducting bend experiments in the temperature range RT to ~400°C if an environmental chamber is available. Low-temperature tests may be considered but are not verified at the present.

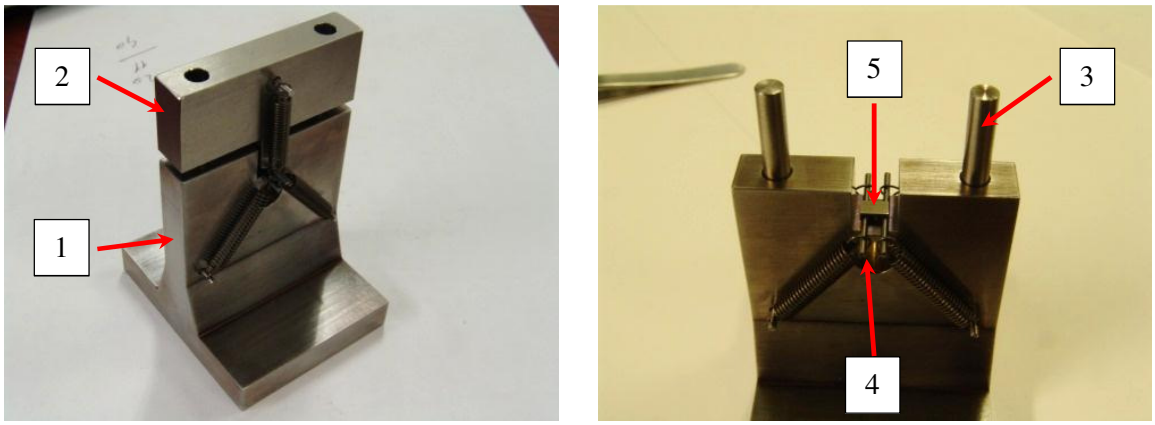

Fig.1. General view of bend test assembly (at the left); sample in the work position (at the right). 1 – matrix; 2 – punch; 3 – guide rod; supporting rod; 5 – specimen.

The assembly allows for conducting 3- or 4-point tests, depending on a particular goal (see Fig. 2). Span distance is 3.77 mm for 1.23 mm rods, but the matrix design allows also ~8mm span distance if necessary. Virtually any test machine may be used to conduct bend experiments. In the present work, all experiments (except few test loads) were conducted with a MTS one-column tensile screw-driven machine (model Insight 2-52; load capacity 2kN). Currently, all bend experiments were conducted at room temperature. Mobile beam speed during bend tests was 0.1 mm/min that provided strain rate of ~10^{-4} s^{-1}.

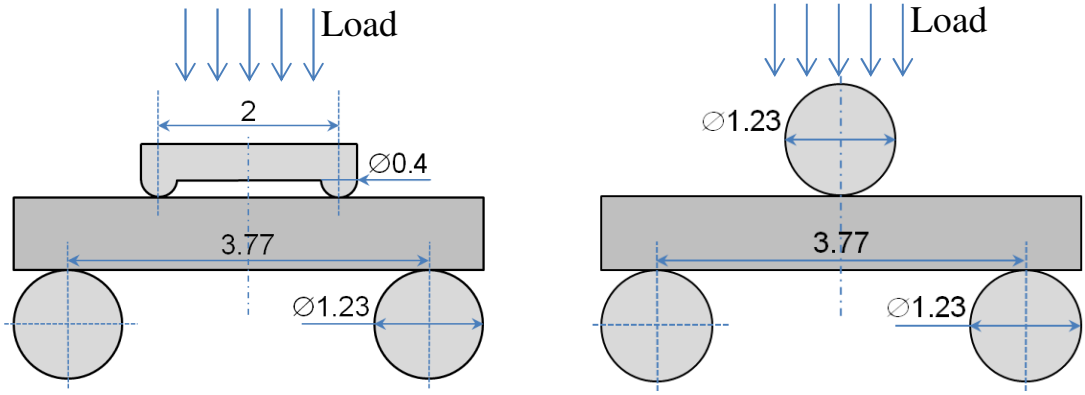

Fig.2. Schemes of 4-point (left) and 3-point (right) bend test assemblies (dimensions are in mm).

An important feature of the designed assembly is an ability to conduct optic observation of the specimen and non-contact measurements during the experiment (see Fig. 3). The specimen may be observed from both side and bottom surfaces (see Figs. 4, 5). In the latter case, high-quality prism is being used to provide bottom surface observation. In general, both digital moderate-

resolution camera for general view and strain measurements and long-focal microscope for detailed view with high magnification may be used simultaneously.

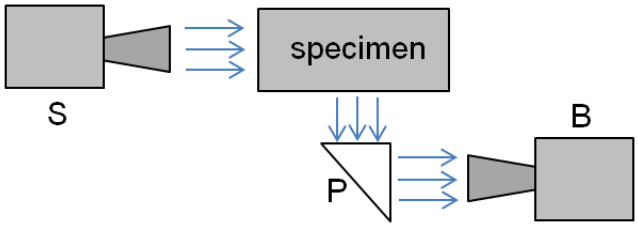

Fig. 3. Observation of the specimen with side (S) and bottom (B) cameras. High-quality prism (P) is being used to provide the bottom surface observation.

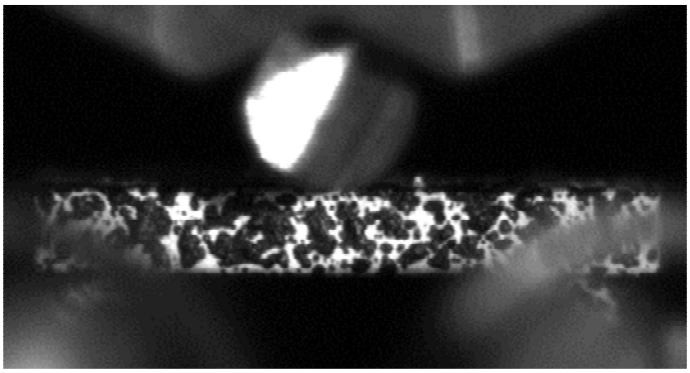

Fig. 4. An example of side view with random speckle pattern. Red arrow shows the specimen.

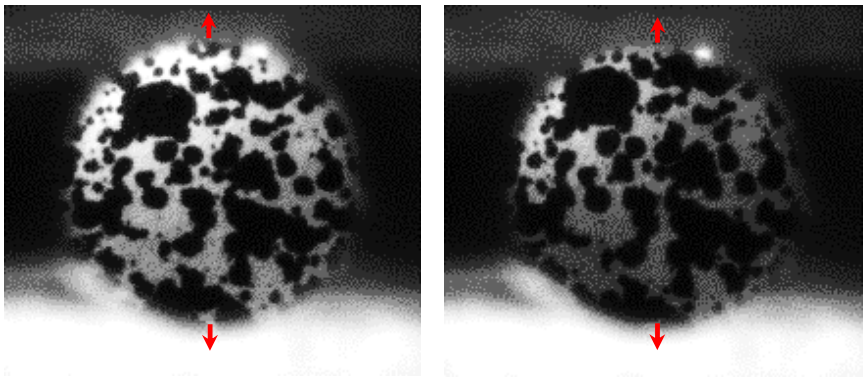

Fig.5. Bottom surface view before and after 3-point test.

2.2. Material investigated

In the present work, 3- and 4-point bend experiments were conducted for a set of non-irradiated and irradiated austenitic (304, 316, some model alloys bases on 304 steel) and ferritic (F82H, A533B) steels. The tested materials are listed in the Table 1.

Irradiated model alloys used in this study (see Table 2) were modifications of high-purity commercial AISI 304 stainless steel. The alloys were produced for a cooperative program of IASCC research [1]. During this program, more than 10 modified steels and alloys were produced, irradiated and used to characterize IASCC [2]. Specimens for the present work were small plates with dimensions 5 x 3.5 mm and nominal thickness of 1.2 mm. The specimens were cut off the end of irradiated tensile bars. The bars were irradiated in the BOR-60 fast reactor to 4.4 dpa at 593K and an average dose rate of ~8×10^{-7} dpa/s [2].

Table 1.

List of materials subjected to 3- and 4-point bend tests

Material	3-point test	4-point test	Purpose
Non-irradiated.			
F82H steel	Yes	No	Tensile-bend properties correlation; general performance of the system.
A533B steel	Yes	No	Tensile-bend properties correlation; general performance of the system.
Industrial grade of 304&316 steels.	Yes	Yes	Tensile-bend properties correlation; general performance of the system.
Model alloys A,E, F, G, K, P.	Yes	Partly	Phase and structure transformations; tensile-bend properties correlation.
Irradiated.			
Model alloy A	Yes		Phase and structure transformations in the irradiated materials; deformation localization.
Model alloy E			
Model alloy H			
Model alloy A		Yes	Deformation localization and dynamics of dislocation channeling in irradiated austenitic alloys.
Model alloy E			
Model alloy H			
Model alloy K			
Model alloy SW			

Model irradiated and non-irradiated austenitic alloys also were used to investigate phase and structure transformations (twinning, martensitic transformation, mainly 3-point bend test) and deformation localization dynamics (channeling; mainly 4-point bend test). Some of the most interesting results will be discussed below.

Ferritic and industrial grade austenitic steels were used to investigate general performance of the system: relationship between crosshead speed and strain rate on the sample surface, the range of loads for different strength materials, strain distribution along the surface, etc. Also, these

materials and some high purity alloys were used to build a correlation between yields stress during tensile and bend tests.

Table 2.

Damage dose, element composition (wt. %)*, and grain size for investigated irradiated model alloys

Alloy	Max. dose, dpa	C	**Mn**	**Si**	**Cr**	**Ni**	**Mo**	N	Grain size, μm
A	47	0.023	1.82	0.56	19.95	10.8	0.53	0.072	38
E	11.8	0.021	0.94	0.04	18.76	12.37	0.04	0.0003	48
H	7.8	0.02	1.01	1.05	18.17	12.45	0.02	0.0005	32
K	9.6	0.02	1	0.03	18.21	25.08	0.02	0.0005	24
SW	4.4	0.022	1.07	0.24	18.42	10.45	n/d	0.025	67

* In all alloys: P<0.01%; S<0.01%; Ti < 0.02; Nb < 0.005. The P alloy also contains 1.17% Hf.

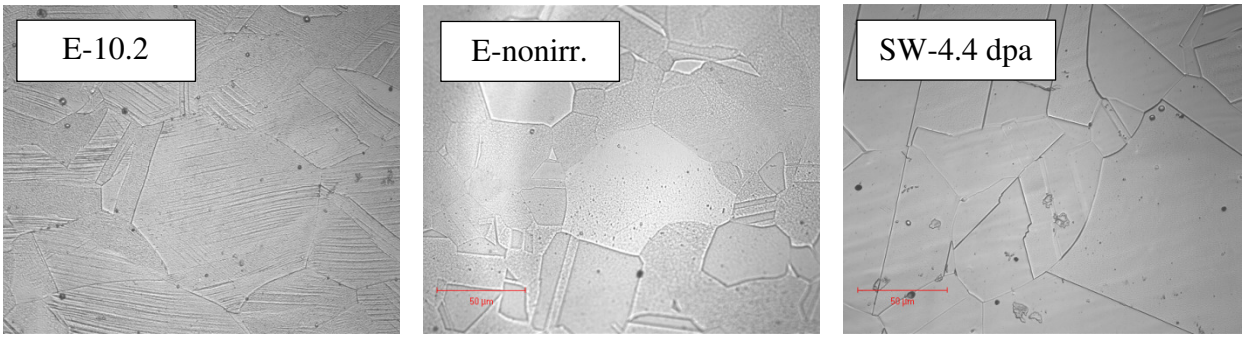

Fig.6. Typical metallographic structure of investigated irradiated alloys illuminated by etching with 10% oxalic acid at 6V for 60-80 sec. The magnification is the same for all images.

Prior to the deformation experiment, irradiated specimens were mechanically polished from both sides and ~200 microns were removed from the surface using standard metallographic procedures. To get a clear defect free surface, electro-polishing was conducted using a Struers unit with standard A2 electrolyte. To reveal grain structure (see Fig. 6), the samples were slightly etched with 10%-oxalic acid at 6V DC and after that electro polished for 2 sec to remove any etching products. The final thickness of the specimens was 0.8 mm.

2.3. Optic non-contact strain measurements

An Allied Vision Technology GX3500 digital camera was used to obtain images of specimen surface during bend experiments; resolution was ~10 μm per pixel. To calculate strain field and

measure displacements, VIC-2D commercial software and a custom program was used. The method, named optic extensometry or digital image correlation (DIC), is described in detail elsewhere [3, 4]. DIC allows one to measure as small strain as ~0.01%, but exact result depends on imaging condition, light, specimen surface, etc. Since DIC plays a secondary, supporting role in the present work, it will not be discussed here.

2.4. In-situ optic microscopy

Keyence VHX-1000 digital microscope with long-focal lens was used to obtain high-resolution images of the surface during bend experiment (see Fig.7). The custom-built bend assembly (see above) included special high-quality prism which allowed in-situ observation of the bottom surface of the specimen with magnification up to 1000x.

Video record obtained during the experiment was analyzed frame by frame using custom program that allowed tracking individual slip lines and dislocation channels and analyzing their dynamics (origin points, propagation direction, sequence of channels appearance, etc.). Usual video frame dimensions were ~800 by 600 μm, and a typical number of grains in the observed area was ~100-400 depending on the material.

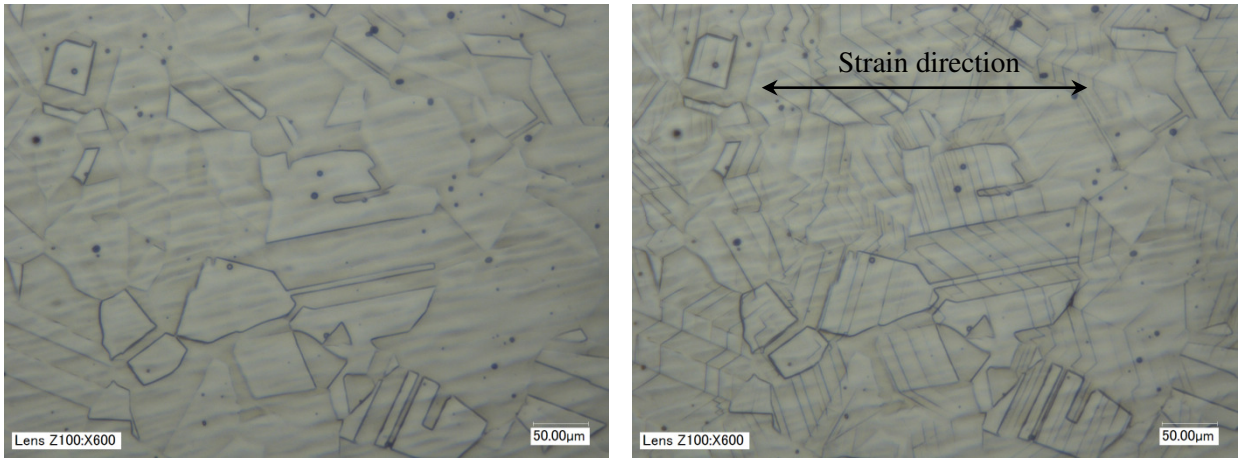

Fig. 7. The same area before loading and after loading to 1740N, SW-alloy (industrial high-purity 304 SS), 4-point test. 0.8% strain. One may see numerous dislocation channels.

2.5. Magnetometry

Some of materials listed in Table 1 are metastable (for instance, alloys E, F, SW, etc.) and magnetic bcc-phase can form during both irradiation (ferrite) and deformation (martensite). To control the amount of magnetic phase in the bulk specimen, a Fisher FMP-30 Ferroprobe was employed. Prior to measurements, the device was calibrated with a three-level ferrite etalon set

at 0.53%, 2.96%, and 10.4% of δ-ferrite. This Ferroprobe has a threshold limit of 0.1% of ferrite, any magnetic phase amount below this limit could not be reliably detected. However, if the amount of magnetic phase exceeds 0.1%, the smallest detectable change is ~0.02%.

2.6. Electron backscattering diffraction

Scanning electron microscopy was performed using a JEOL JSM 6500F microscope with a field emission gun (FEG), equipped with an EBSD system. The accelerating voltage was 20 kV, and the working distance between 12 to 15 mm; the EBSD maps were measured on a hexagonal grid with a step size of 0.1 to 2 μm. The camera ran at ~50 frames/s in 4x4 binning mode during regular scanning and in 1x1 binning mode (averaging up to 20 frames) during phase analysis and pattern identification.

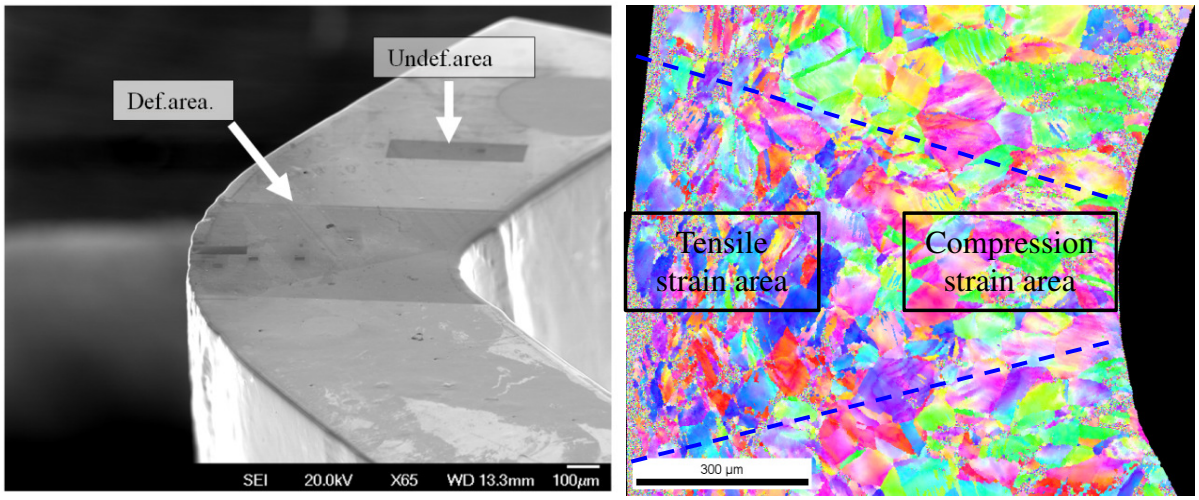

Fig. 8. Left: Irradiated bend specimen (E-alloy, 10.4 dpa) prepared for SEM-EBSD. Right: low-magnification EBSD scan showing both tension and compression areas; note the difference in color caused by stress state influence on the development of texture.

Prior to EBSD analysis, the bend specimens were cut along the center line and the cross-section area was prepared using routine metallography procedures. Prepared specimen (see Fig.8) contains both non-deformed and deformed areas. The deformed area has locations with different stress and strain values. The stress and strain distribution may be revealed by FEA; this aspect will be discussed below.

3. Experimental results

3.1. Primary experimental curves

Fig. 9 shows an experimental bend curve in “deflection, mm – load, N” coordinates. As one can see, this bend curve, by analogy with tensile one, includes elastic and plastic parts. For more detailed analysis, it is convenient to subtract the elastic deformation and operate by the plastic deflection only. Also, experimental bend diagrams in many cases are a little wavy probably due to some effects connected to dry friction.

To compare samples of different thickness, one can convert load value to more universal bend stress parameter. In the present work, bend stress σ_b was calculated using a common relationship $\sigma_b = (3 \cdot F \cdot d)/(2 \cdot W \cdot T^2)$ where d is span distance (3.77 mm) and W is sample width (typically 3.5 mm), and T is sample thickness (varied 0.6 to 1.1 mm). Obviously, this relationship should be used carefully for experiments where large plastic strain exists.

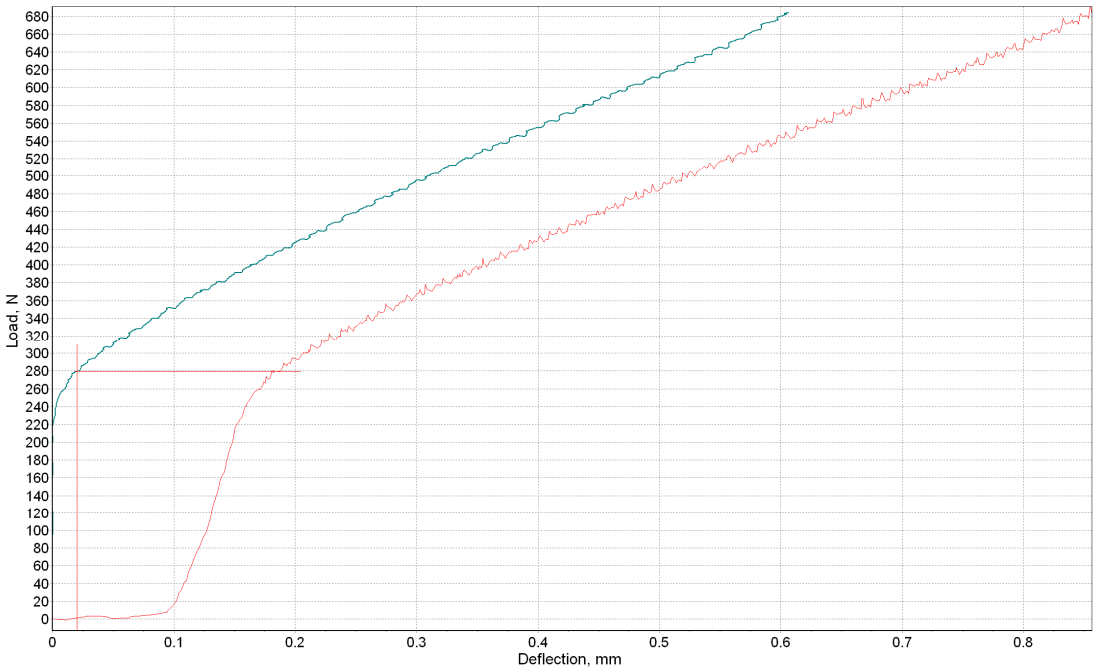

Fig. 9. Experimental curve “deflection, mm – load, N” for non-irradiated sample of A-alloy.

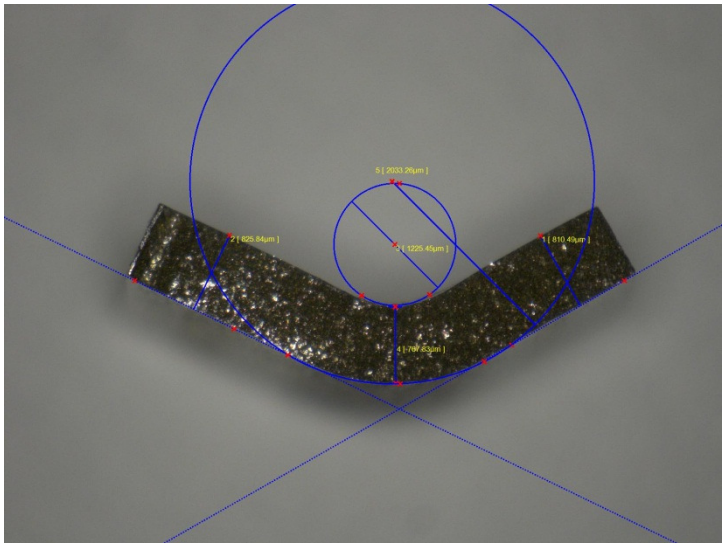

Fig. 10. Specimen after bend test (A-alloy). View from the top (3D confocal image). See also Fig. 8 with specimen prepared to SEM-EBSD analysis

Fig. 10 demonstrates typical view of specimen after 3-point bend test. One can see that strain distribution has relatively non-uniform character; the most deformed part is located close to the load axis, and deformation decreases fast along the bottom surface.

Fig. 11 shows bend diagrams obtained for irradiated specimens. Comparing to the tensile test case, bend diagrams for irradiated samples are relatively long and do not demonstrate a tendency to early necking and force drop. Early necking is a typical phenomenon in tensile-deformed highly-irradiated stainless steels, but necking in its usual form was not observed during bend test in the present work; load increased continuously during 3-point bend experiment until maximal allowable deflection (~1.1 mm) was reached.

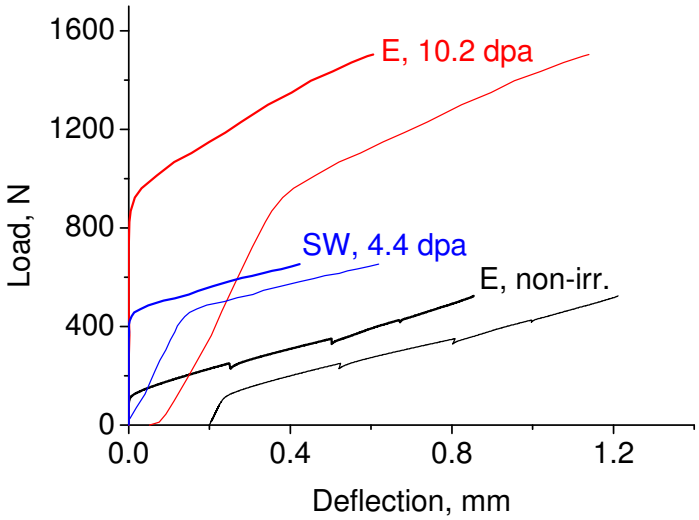

Fig. 11. Typical bend curves in coordinates "Load, N – full deflection, mm" (thin lines) and "Load, N – plastic deflection, mm" (thick lines). Few dents on the bend curve of E-alloy are caused by test interruptions for magnetic measurements. The samples had a different thickness. Some curves are shifted to make the picture clearer.

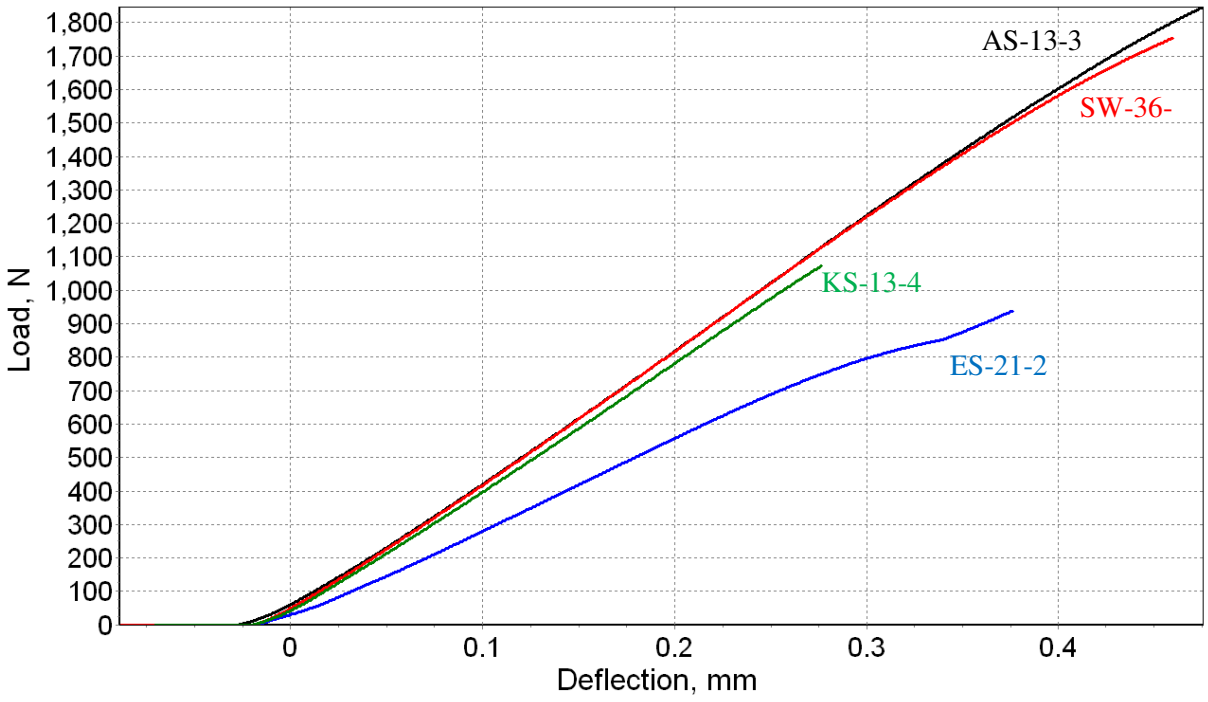

Fig. 12. Load-deflection curves obtained during 4-point bend test of irradiated samples.

Fig.12 shows load – deflection curves obtained during 4-point bend experiments. Since the goal of the experiments was to get relatively small strains, the curves consist of elastic area, which dominates, and relatively small plastic deformation. ES-sample demonstrates some peculiarity of unclear origin.

3.1.1. Relationship between bend and tensile yield stress

The present work did not aim to get any property-property correlation; the only goal was to get a deformed object with well-defined history. However, limited correlation analysis (bend test vs. tensile) was conducted.

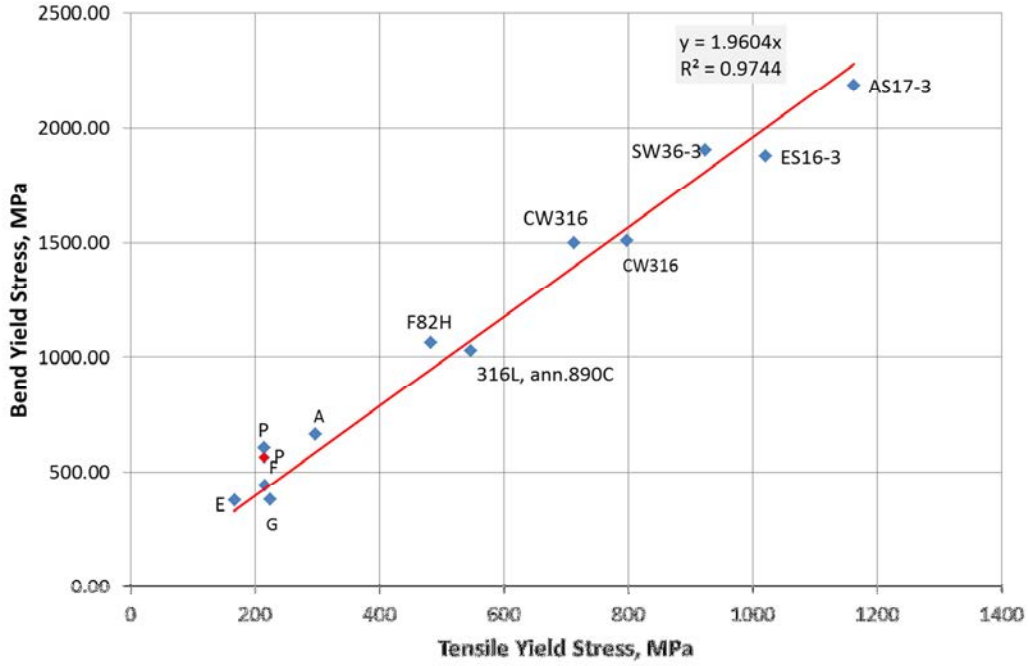

Fig. 13. Relationship between tensile and bend yield stress. Bend yield stress was defined as stress corresponding to plastic retain deflection of 0.02 mm.

Figure 13 demonstrates a correlation between bend and tensile yield stress. One can see that for a set of materials tested there is good linear relationship between tensile and bend test parameters. However, note that the present work did not aim to get any property-property correlation [5]; the only goal was to provide a way to the investigation of deformation modes and strain-induced phenomena using small non-standard specimens.

3.2. Finite element analysis of bend test

In the present work, finite element analysis was used for three main purposes. Firstly, it was interesting to estimate mechanical behavior of high irradiated steel under bending and to establish shape change, possibility of neck formation and its expected location and geometry. Second, it was important to investigate stress and strain distribution and strain gradients across

the deformed area; this was especially important for 3-point bend test. Third, 4-point bend test and dislocation channels dynamics investigation required an estimation of stress along the bottom surface. Finite element modeling task is in progress, and this section represents current preliminary results.

In the present work, commercial FEA software (COMSOL Multiphysics 4.0) was used to model bend test experiments.

3.2.1. Finite element models

Two kinds of finite element models were developed and used for both 3-point and 4-point tests. The first type included two-dimensional (flat) models, which were used to evaluate elastic behavior of the specimen and investigate small plastic strain area (~0 - 0.02). In general, calculation time for 2D models (see Fig.14) is significantly smaller and their spatial resolution (number of elements along any direction) is higher than for 3D, but 2D models do not provide accurate results for large strains.

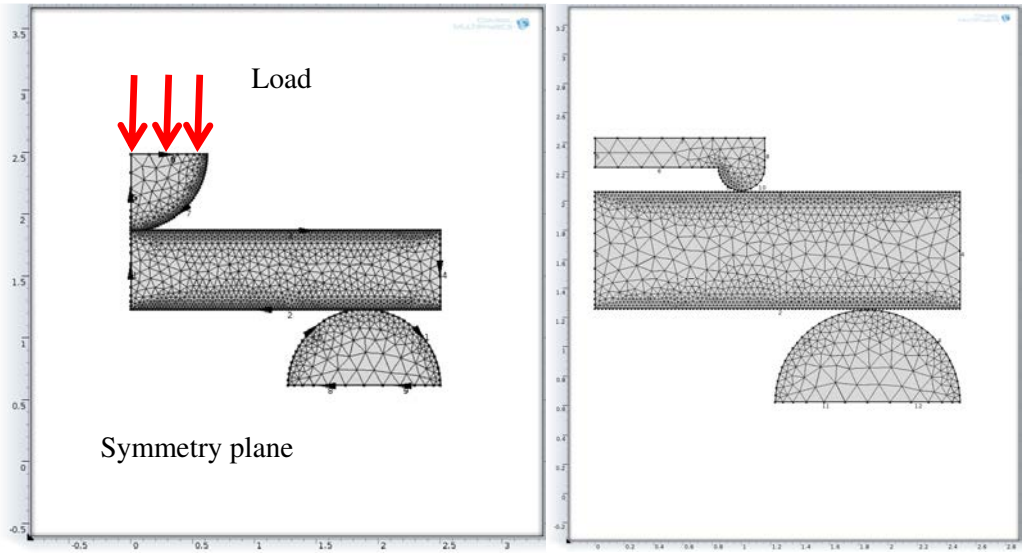

Fig.14. General view of 2D models for 3-point (left) and 4-point (right) bend test simulations.

The second models type was 3D models (see Fig. 15); the 3D models can handle large strains and take into account specimen bending; however, the third dimension drastically increased solution time and in the present work the use of 3D models was limited. To keep reasonable calculation time (tens of hours on desktop PC), one has to limit the number of elements and use 6 to 10 element across the central area (compare Figs. 14 and 15).

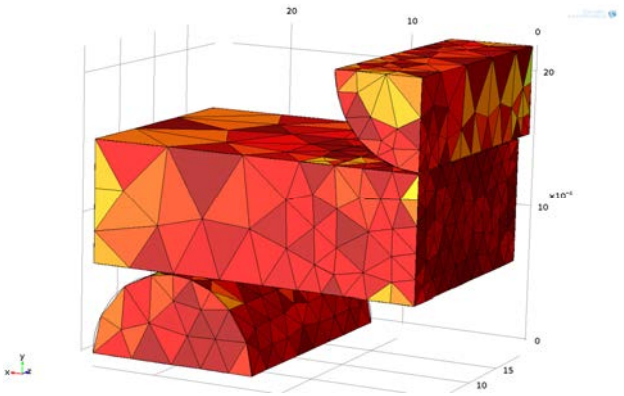

Fig.15. 3D model of bend test experiment. The model includes only 1/4 of the bend assembly because of two symmetry planes.

Elastic parameters were the same for all materials (Young modulus 200e9 GPa, Poisson's ratio 0.3). To model deformation hardening behavior, modified Swift equation [6] was employed:

$$\sigma = k(\varepsilon - \sigma_0^2/k^2)^{0.5} \quad (1)$$

where k is a deformation hardening parameter, and σ_0 is a parameter close to yield stress (for instance, k= 1300 MPa and σ_0=924 MPa for SW-alloy). As one can see, the equation represents parabolic hardening behavior model without hardening saturation. Preliminary values for both parameters were defined earlier using ball indentation method and conventional tensile test coupled with DIC.

3.2.2. Calculated strain and stress distribution in the small strain area.

Stress and strain calculations were performed for most of tested bend specimens to estimate the geometry of deformed area. Figures 16 and 17 shows a typical distribution of stress and strain for 3- and 4-point test cases respectively. One might expect to see compressive and tensile stress areas (top and bottom respectively) and the simulations reproduce these areas accurately.

Plastically deformed area has relatively small size for 3-point test case, and its volume does not grow significantly as load increases. The area is an analogy of stable neck observed during tensile test, but compared to the tensile test case, the location of neck is known before test. Plastically deformed area has strain gradients along the surface also as in depth; however, 3-point bend allows one to reach large deflections (and strain level) without overloading the assembly.

4-point bending provides relatively wide area with uniform strain; the center part of the sample experienced relatively uniform deformation, but in-depth strain gradient cannot be avoided.

After strain level reaches ~0.5-1.5% (an exact value depends on material), deformation begins to localize in two narrow areas located under the top rods (see Fig. 18). This process is also similar to necking observed in the more common tensile test.

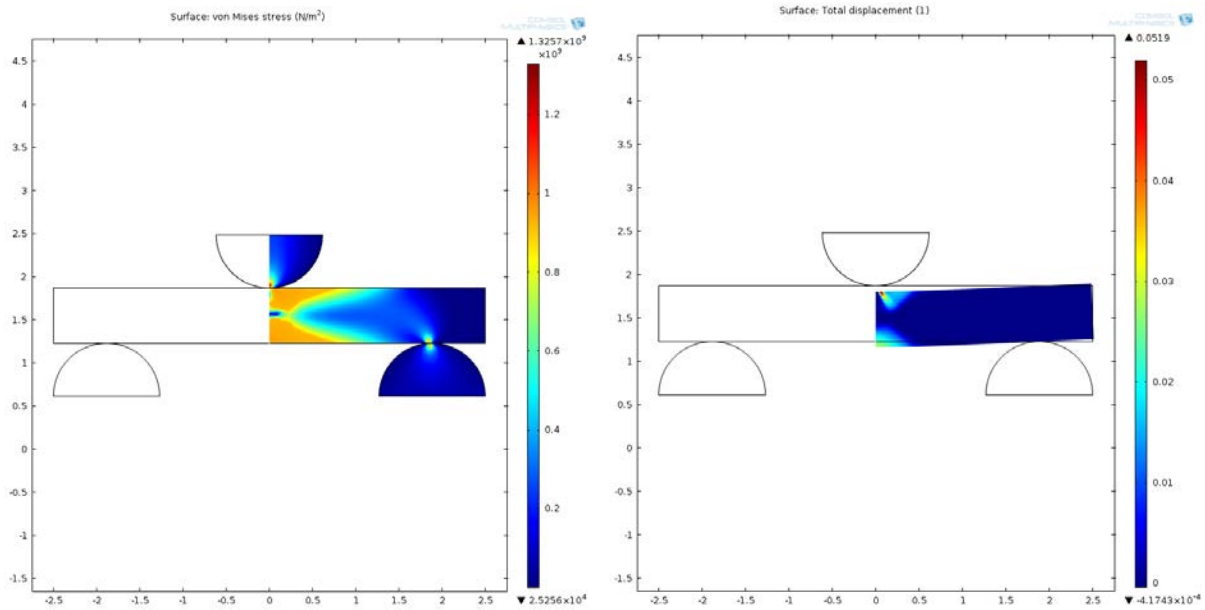

Fig 16. Calculated stress (left) and strain (right) distribution for irradiated AISI 304 steel (SW-36 sample). Total deflection 0.070 mm, plastic deflection ~0.047 mm.

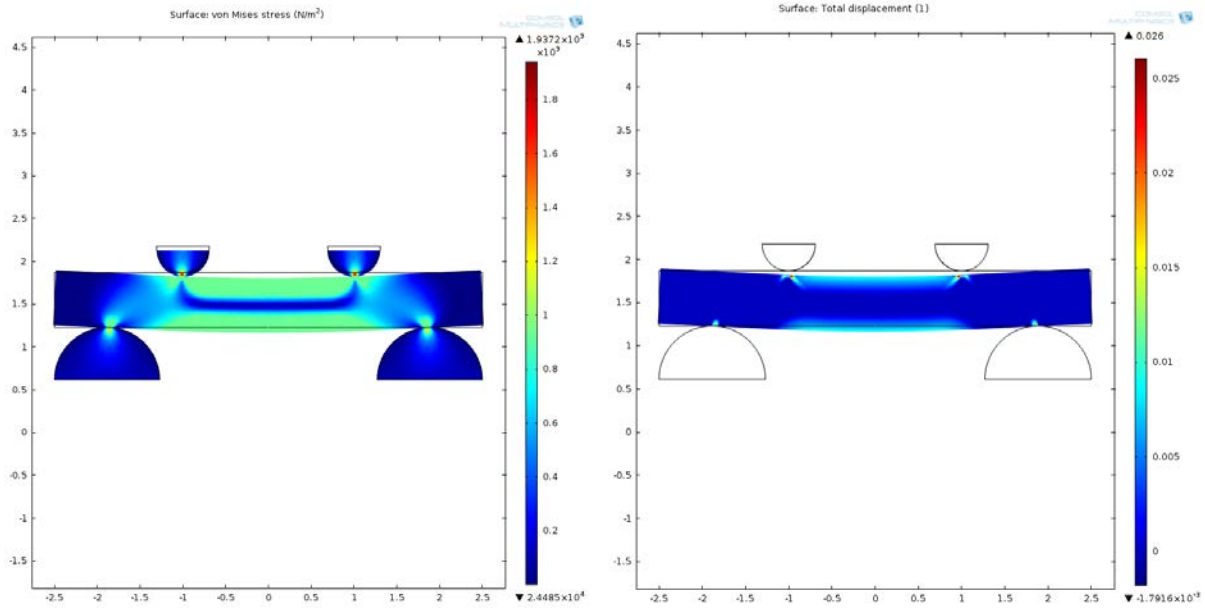

Fig. 17. Calculated stress and strain distribution for future 4-point bend test. Irradiated SW36 sample.

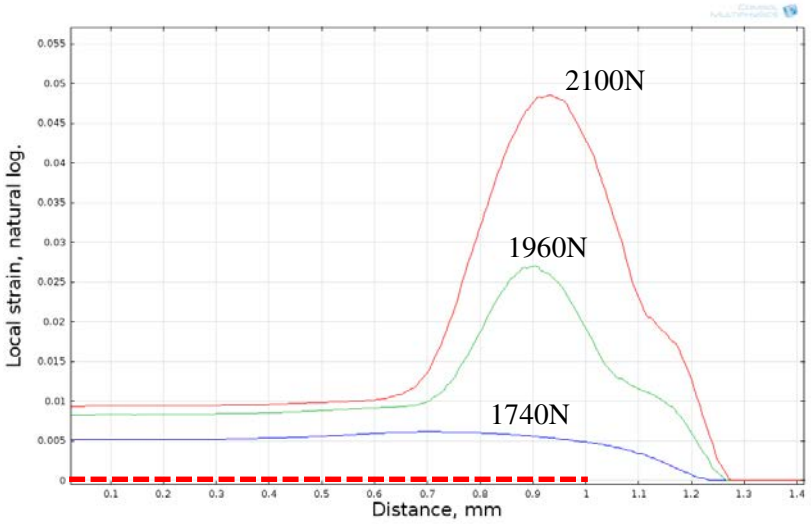

Fig. 18. Computed plastic strain distribution along the bottom surface for different load values. ES-alloy, 11.8-dpa sample.

FEA calculations predicted high strain gradients in 3-point bending and specific double necking effect in the 4-point; these predictions agree with experimental results.

3.2.3. Large strain area and simulated load-deflection curves.

FEA allows one to get simulated "load – deflection" curves if calculation time is not an issue. The goal in this case is to achieve the best similarity degree between real and simulated curves; when an acceptable agreement is achieved, one can assume that simulated stress and stress distributions are also close to the experimental ones.

Fig.19 shows experimental bend curve and few calculated curved obtained as a result of consecutive iterations. As one can see, the first iteration provided unsatisfied results, and material behavior model (k and σ_0 parameters) was modified. The second iteration (coarse mesh was applied to speed-up the process) demonstrated good fitting, and the third iteration with slightly modified parameters and fine mesh demonstrated good agreement with experimental curve.

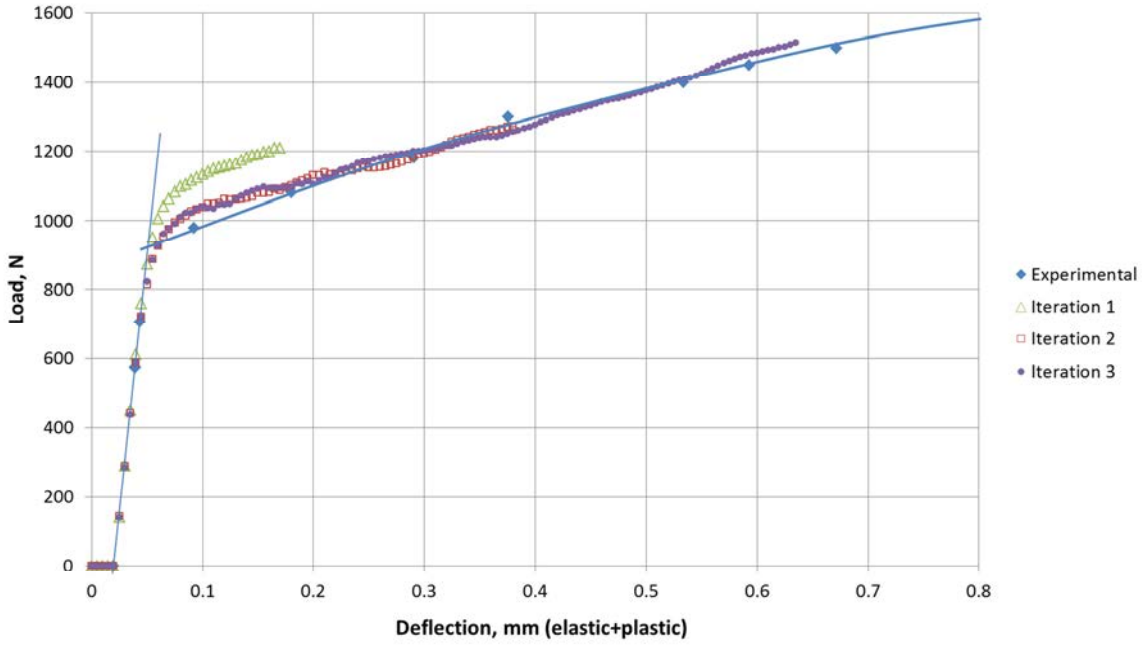

Fig. 19. Experimental and simulated 3-point bend curves for irradiated E-alloy. 3D model (see Figs.15 and 20).

Simulated curves have insignificant sinusoidal-like deviations from pure deformation hardening; most probably, the deviations caused by relatively large elements size at the rod-specimen contact points (see Fig. 15). Friction also can play a significant role; the changes of friction coefficient did not influence the simulated "load-deflection" curve, but insignificantly affected sinusoidal-like force fluctuations.

It is interesting that FEA simulation of large strain area predicted a specific bending effect at the edge of the specimen (see Fig. 20). Later this phenomenon was observed in the deformed irradiated and non-irradiated specimens.

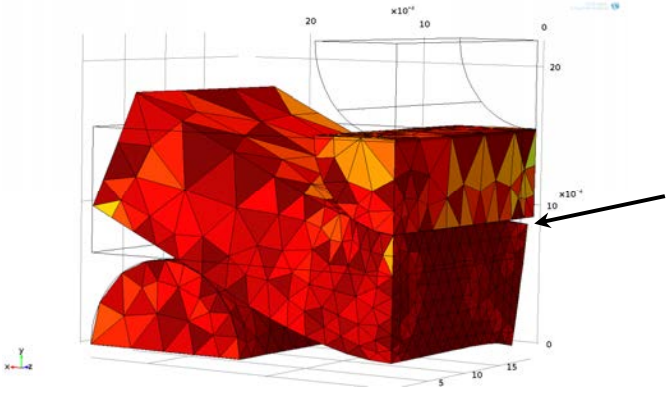

Fig. 20. Deformation and bending (shown by the arrow) at the edge of the specimen. Compare with Fig.15 (non-deformed mesh).

3.3. Deformation modes in irradiated austenitic stainless steels

Plastic deformation of austenitic steels is a complex multi-modes process which includes ordinary dislocation slipping, deformation twinning, deformation martensitic transformations (fcc→to hcp and/or fcc→bcc), and some other phenomena. Each of these phenomena can play a positive role and may be used in practice (TRIP, TWIP steels); however, in many cases they may have a negative impact on material performance (hydrogen embrittlement of bcc-phase, etc.).

Irradiation leads to defects accumulation, microstructure and microchemistry evolution, and therefore strongly influences deformation modes. For instance, numerous dislocation slip lines disappear and evaluate to coarse and narrow dislocation channels; twinning may happen almost at zero strain or even below the yield stress limit, not at high strain as in non-irradiated material.

Instead of a high number of published papers, many aspects related to deformation behavior of irradiated materials remain not well uninvestigated. This section presents some results on describing deformation modes in irradiated austenitic steels.

3.3.1. Phase and structure transformations in irradiated material

Austenitic stainless chromium-nickel alloys are widely used in the nuclear industry as a constructional material due to good combination of strength, corrosion resistivity and other properties. Some of the chromium-nickel alloys are metastable, and a martensitic transformation can take place during plastic deformation. Appearance of martensite in the structure can change mechanical behavior of the material and generally improves its strength. Besides the strength, formation of martensite can change other properties of the material. For example, in bcc-phase the binding energy between hydrogen and a trapping site is considerably lower than in fcc, and the rate of hydrogen diffusion can be 5 to 10 times and more high depending on applied stress and other conditions. One can expect the presence of martensite in structure, especially near of the grain boundaries, can increase hydrogen transfer rate and accumulation of hydrogen near of crack tip. Also, it is shown that pit propagation in AISI 304 stainless steel may accelerate with increasing martensite content.

Different aspects of the martensitic transformation (effect of alloying, stress state, etc.) are widely discussed for non-irradiated alloys, but a few papers exist for irradiated steels. In this section, we present results on martensite formation in irradiated austenitic steels.

3-point bend tests were conducted with specimens of alloys SW, E, A, and some other. Primary experimental load-deflection bend curves were discussed above and Fig. 21 shows calculated bend curves in coordinates “Bend stress, MPa – plastic deflection, mm”. One can see that the

use of bend stress parameter, instead of load, eliminates the difference in samples geometry and allows one to compare different alloys easier. For instance, one can see that curves for E and SW-alloys samples are located close to each other as would be expected from their strength level.

Also, Figure 21 shows the magnetometer readings as a function of plastic deflection. One can see that the amount of magnetic phase begins to increase after some plastic deformation, and martensite in irradiated alloy SW accumulates faster than in E. At the same time, non-irradiated alloy E did not show any magnetic phase accumulation during bend test. Due to limited allowable deflection value (~1.1 mm for the given bend assembly), maximum strain in the deformed area did not exceed ~0.3, whereas formation of martensite in this alloy takes place if strain exceeds ~0.35.

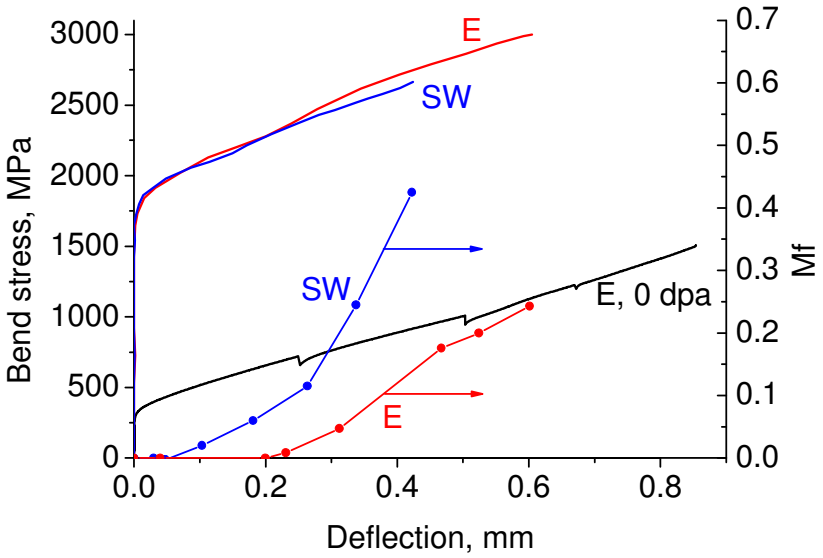

Fig. 21. Plastic deflection versus bend stress (thick lines) and magnetic phase amount (thin lines with markers). Non-irradiated E-alloy did not show any increase of magnetic phase amount during bend test.

It is well known that martensitic transformation in the case of tensile deformation can be characterized by critical stress (σ_{CR}) and critical strain (ε_{CR}) parameters; martensite during plastic deformation begins to accumulate when stress and strain exceed these critical levels. In the past, both of these parameters – stress and strain – were considered to be equally valuable, but in the last few years the martensitic transformation is often treated as a stress-driven process.

As follows from Fig.21, martensite begins to form in SW-alloy at the plastic deflection value ~0.06 mm and E-alloy at ~0.22 mm. The measured strain values on the surface were ~0.08 and ~0.2 respectively. It is possible to conclude that critical strain required producing martensite

decreases significantly during irradiation (from ~0.4 to ~0.2 in E-alloy); at the same time, irradiated alloys still require some plastic strain to produce a detectable amount of martensite. For the irradiation conditions studied in the present work, critical strain, which needs to be reached to provide martensite formation in the volume of the specimen, did not reach zero value.

Yield stress for tested irradiated samples (~900-1000 MPa) exceeded typical critical stress required for martensite formation in similar alloys (~550-600 MPa); therefore, it was possible to expect that some martensite amount will form below the yield stress ("elastic" or "stress-induced" martensite). However, no detectable change of magnetic signal was observed during elastic loading of the samples.

Fig. 22 shows volume amount of martensite as a function of true strain and stress. Martensite amount was measured with EBSD in different areas along the cross-section of bend specimen. True stress and strain values were obtained from FEA (see above); strain value at the surface of the specimens was confirmed also by DIC measurements. Each point for non-irradiated alloy shows averaged data of at least 5 EBSD scans for different areas, at the same time, only one scan was available for each strain level for irradiated samples.

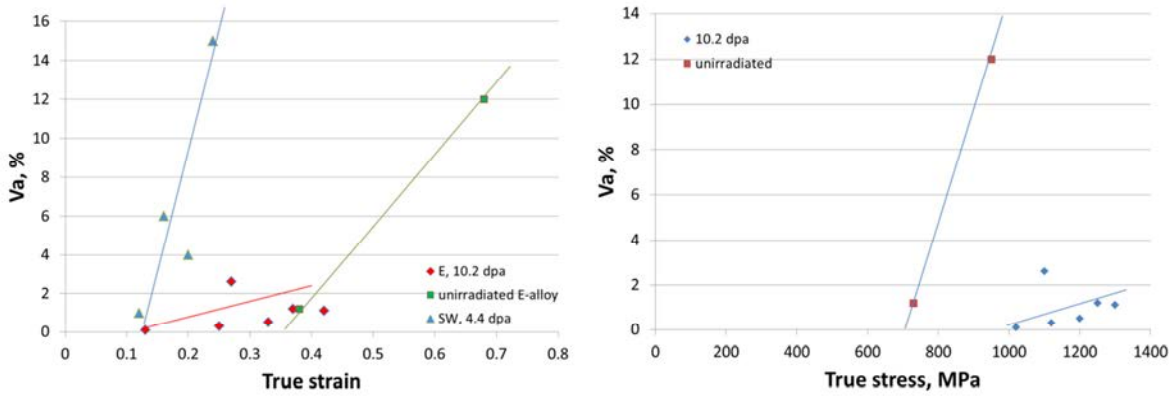

Fig.22. Martensite amount as a function of true strain and stress.

Table 3.

Parameters of martensitic transformation
(critical strain ε_{cr}, critical stress σ_{cr} and intensity K_α) for investigated alloys

Alloy	SFE, mJ/m^2	Ni_{eq}, %	Non-irradiated			Irradiated		
			ε_{cr}	σ_{cr}, MPa	K_α	ε_{cr}	σ_{cr}, MPa	K_α
SW	22.1	24.2	-	-		~0.1	~1050	
E	28.7	25.9	0.35	700		~0.15	~1100	

As follows from the Figure (see also Table 3), martensite in irradiated E-alloy begins to form at ε~0.1 whereas in non-irradiated at ε~0.35. True stress required for the formation of martensite is ~1000-1050 MPa which is significantly higher than in non-irradiated (~700 MPa). It is possible to conclude that neutron irradiation significantly decreases critical strain and increases critical stress required for martensite formation in the volume of the specimen.

3.3.2. Morphology of deformation twins and martensite

Figure 23 demonstrates the typical deformed structure of irradiated and unirradiated specimens. Strain levels differ significantly between irradiated and unirradiated samples; however, stress values are comparable. There was no possibility to achieve a higher level of tensile stress in the unirradiated sample because of specimen rupture during tensile test.

As follows from the structure images, both irradiated and unirradiated specimens demonstrate deformation twinning. The twinning seems to be sensitive to the orientation of a particular grain. For example, in unirradiated material [100]-grains are practically free of deformation twins and [111]-grains demonstrate intensive twinning (see Fig. 23); unfortunately, a detailed analysis is impossible for irradiated material since it already contained twins because of the pre-irradiation cold work. However, some grains contain no pre-irradiation nor post-deformation twins (see grain G_1 in Fig. 23). This finding requires an additional special investigation.

In contrast to twins, deformation martensite appeared in the specimen only after deformation, so martensite formation sites and grain orientation influence can be analyzed in detail.

It should be noted here that both irradiated alloys contained ferrite formed as a result of irradiation. There was no possibility to separate martensite and ferrite. The amount of such radiation-assisted ferrite was ~0.19 vol. % in E-alloy and ~0.34% in SW, which is relatively small compared to the amount of martensite. It was believed that experimental results obtained for martensite are not compromised by the presence of ferrite.

In irradiated E-alloy martensite particles are most often observed on the intersection of slip lines and twins or at the intersection of two slip lines.

Also, one can see that martensite in the irradiated allow is significantly smaller than in unirradiated. In unirradaited alloy, an average size of martensite particle is ~0.6-0.8 μm whereas in irradiated ~0.3-0.4 μm. Large elongated martensite plates, which are typical for the neck of unirradiated sample, were not observed in irradiated E-alloy.

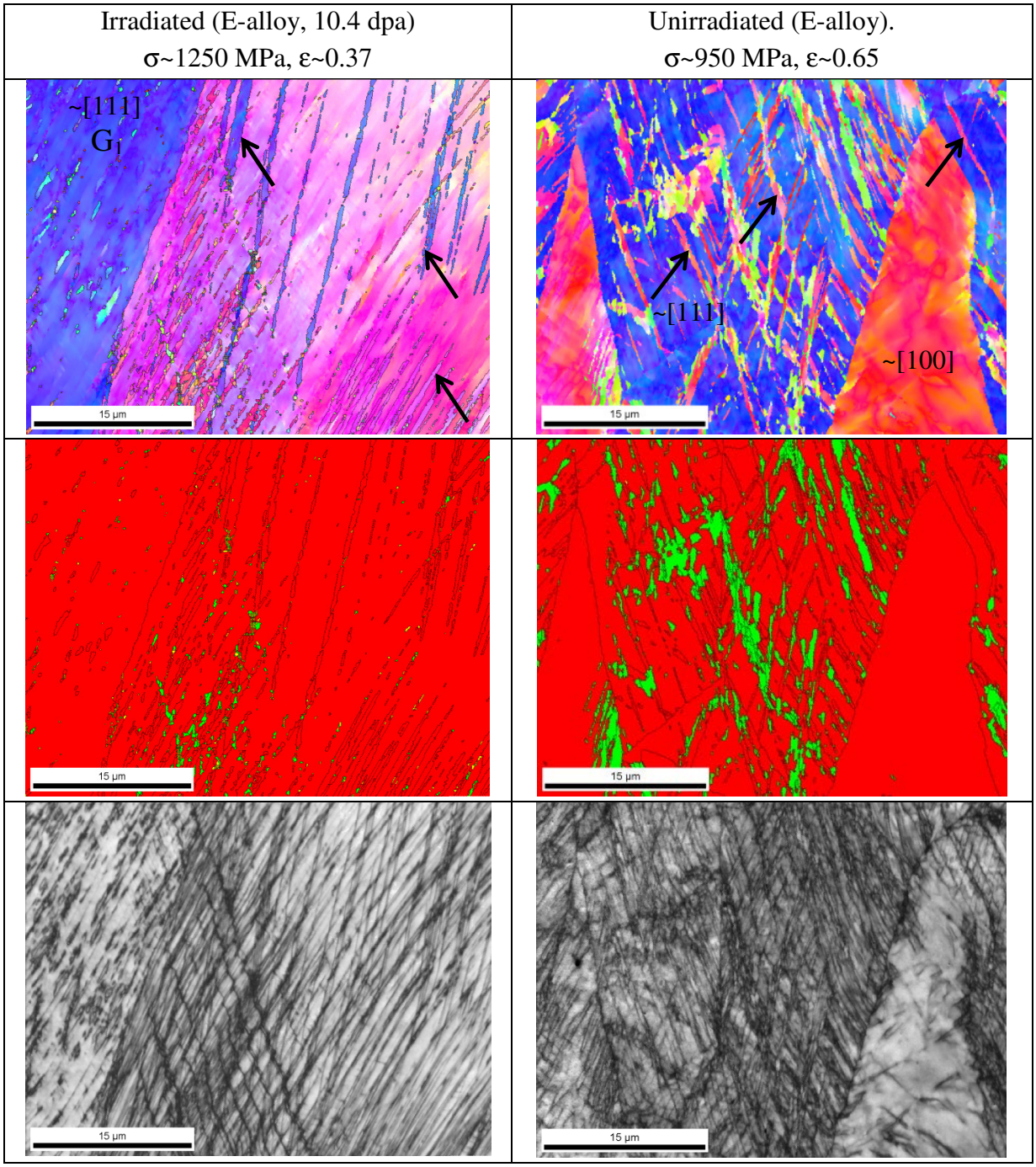

Fig. 23. [100]-IPF, Phase, and IQ maps for the irradiated and unirradiated deformed specimens of E-alloy. Stress and strain values are shown on the top of the Figure. Deformation twins are marked by black arrows. For some grains, their orientation to the load axis is shown. Load axis is vertical.

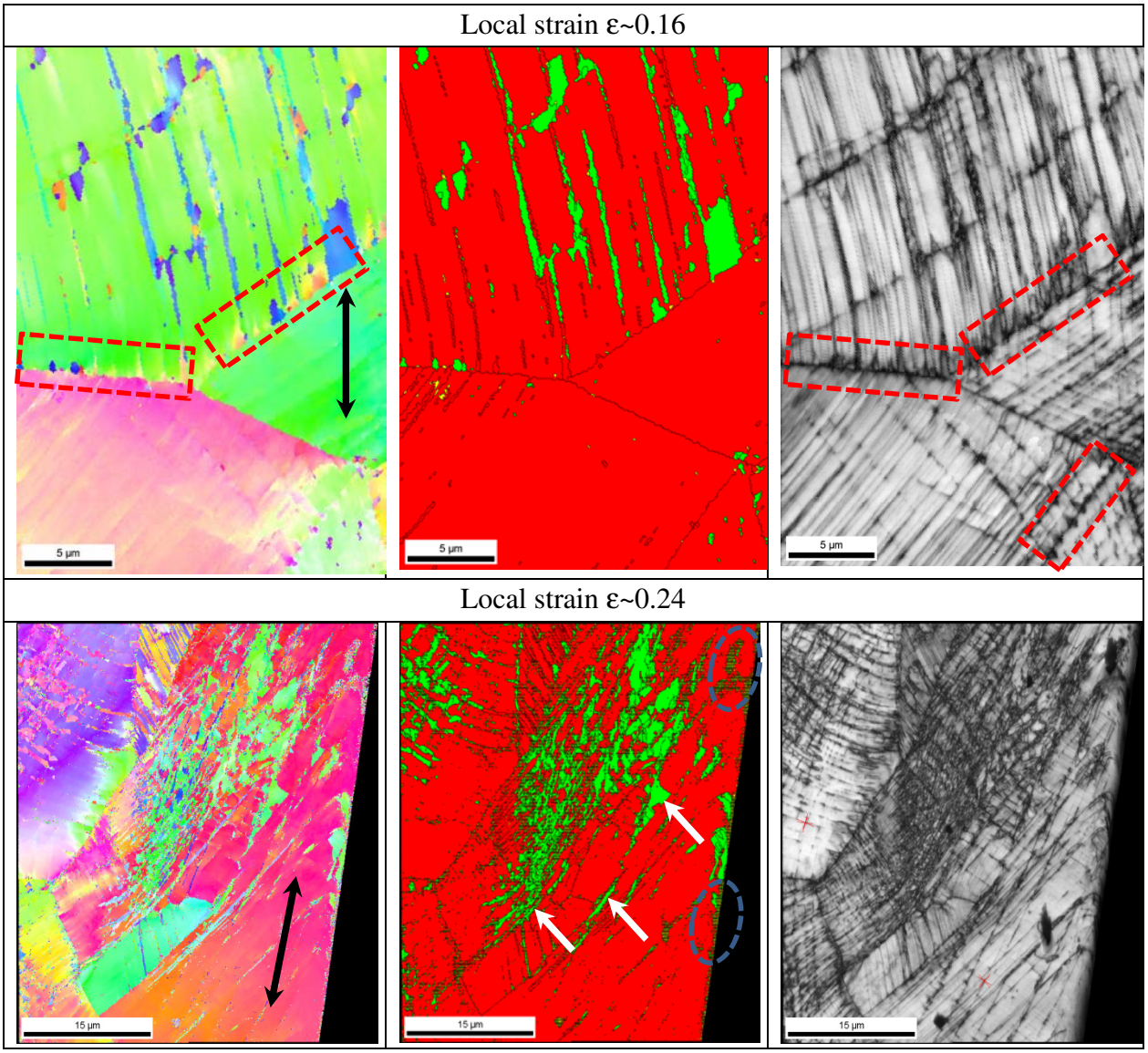

Fig. 24. Typical [100]-IPF, Phase, and IQ maps for deformed SW alloy. Austenite is red, α'-martensite is green. Straining direction is shown by arrow. The bottom scan with ε~0.24 is located close to the edge of the specimen. Step size 0.1 μm. Unindexed areas are shown by dash ovals. Dash rectangles show specific areas of slip line – grain boundary interaction. White arrows show martensite along grain boundaries.

Figure 24 shows the structure of deformed SW-alloy. One can see numerous slip lines and deformation bands, which are believed to be defect-free channels. Intersections of the deformation band with grain boundaries are often visible as a series of dark gray triangles. The same areas in the IPF maps show significant local misorientation. Local misorientations caused by high local density of dislocations are often considered as one of the reasons of irradiation-

assisted stress corrosion cracking. However, a detailed analysis of misorientations in irradiated steels requires a separate paper and will not be considered here.

Deformation α'-martensite forms, as a rule, along deformation bands, at the intersection of deformation bands, or near of grain boundaries. In some cases, specific elongated martensite particles form along grain boundaries (see Fig.24). Also, one can see an inhomogeneity in martensite distribution: martensite forms dense colonies in some grains, but other grains could be almost martensite-free. In SW-alloy martensite particles are significantly larger than in E-alloy.

3.3.3. Deformation localization and channeling in irradiated austenitic steels

High-dose neutron irradiation and post-irradiation deformation of metallic polycrystals lead, as a rule, to deformation localization and formation of dislocation channels. It is generally accepted that most or all deformation occurs in channels, which parameters depend on material, grain orientation and size, stress and strain levels. Recently channeling was identified as a contributor to irradiation-assisted stress-corrosion cracking [7]. In particular, stress corrosion cracks are initiated when average channels height exceeds some critical value [8]. Much work has been done in trying to rationalize the formation and evolution of these channels; nevertheless many questions are not well investigated. For instance, spatial distribution and evolution of the channels, origin sites, interaction with grain boundaries, etc.

In the present work, first steps are taken to investigate channels dynamics during deformation of irradiated metallic polycrystal. By coupling several analytical technics, channels appearance sites, the role of grain orientation, and the spatial channels organization were investigated for 4.4-dpa irradiated AISI 304 stainless steel (SW-alloy, see Table 1). 4-point bend tests were conducted using experimental assembly described above (see Section 2).

Prior deformation experiment the central area of the specimen was characterized using OIM-EBSD. Obtained crystallography information (see Fig. 25) included grain orientation, Schmid factor, elastic stiffness, and grain boundary type. In this alloy, many grains had relatively large size (~100 μm or more) and contained multiple annealing twins. Fraction of "hard" grains with Schmid factor less than 0.3 was about 6%, and "soft" grains with Schmid factor 0.4 or more occupy ~80% of the space. It is important that the grains with the same Schmid factor may have different elastic stiffness value and, therefore, different amount of elastic energy. Since both Schmid factor and elastic stiffness values are sensitive to grain orientation, [111]-grains will have the lowest Schmid factor and highest elastic parameters.

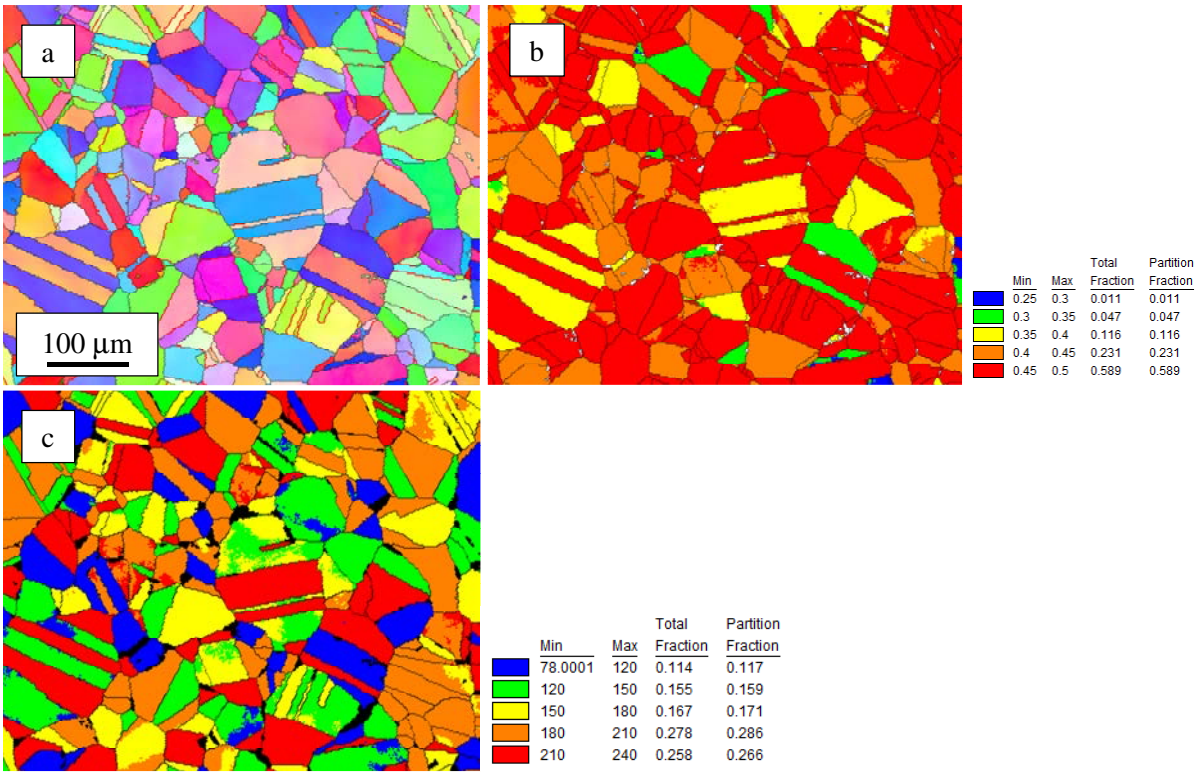

Fig. 25. IPF (a), Schmid factor (b), and elastic stiffness (c) maps for the area of interest. Elastic stiffness map was calculated using the following constants: C_{11} = 232 GPa; C_{12} = 154 GPa; C_{44} = 118 GPa.

According to EBSD analysis, 67% of grain boundaries were random high-angle boundaries (RHAB, misorientation 15 degree or more), 1.2% - random low-angle boundaries (5-15 degree), 30% - Σ3 twin boundaries, and 1.1% - CSL Σ9 and Σ27 boundaries (see also Fig. 26); other GB types (<0.7%) were excluded from the analysis. Such distribution of grain boundaries (~2/3 of RHAB and ~1/3 of Σ3) is typical for annealed 300-series austenitic steel not subjected to any grain boundary engineering procedure, which can increase Σ3 boundary fraction up to ~70%.

As load increased during the test, stress increased also and at stress level of ~670 MPa the first channel was observed (see Fig. 26). This stress level corresponds to ~0.72 of yield stress. Channels formation below the yield stress was observed by many authors. For instance, Edwards et al [9] conducted a detailed investigation of copper irradiated with neutrons and deformed at different strain levels. Defect-free channels were observed in samples, loaded at 270 MPa, which is ~0.84 of macroscopic yield stress (~320 MPa). In many papers, triple junction points are considered to serve as origin points for first channels.

In the present work, the first channel appeared at the middle of grain boundary and was not associated with triple junction points (TJP). Comparing Figs. 25 and 26, it is easy to see that the channel appeared in the “soft” grain (with high Schmid factor) at the boundary with “hard” (low

SF) “stiff” (high elastic stiffness) grain. Channels #2 and #3 also appeared in the soft grains which were close to hard stiff grains. In both cases, the origin points were located in the center of grain boundary far from TJP.

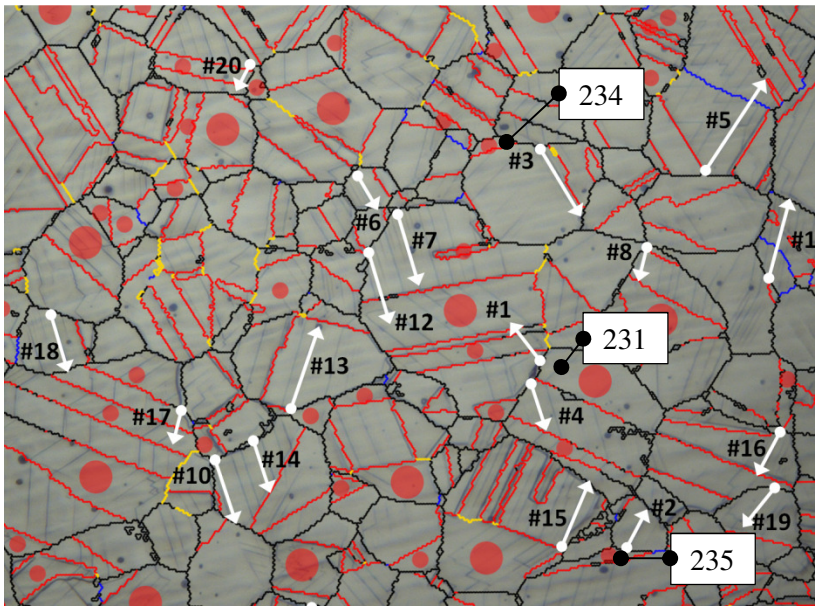

Fig. 26. Optic image of the deformed surface superposed with grain boundary network defined by EBSD. RHAB – black; RLAB – blue; twin (Σ3) – red; CSL (Σ9, Σ27) – yellow. White arrows #1-#20 indicate the origin point and the propagation direction of the first 20 dislocation channels. Stiff grains (with elastic stiffness modulus 210 GPa or more) are marked by red circles. For three stiff grains, their elastic stiffness values are given.

Starting at ~800 MPa channels began to appear at TJPs; however, in many cases these points were close to stiff grains. Figure 27 shows the number of channels as a function of stress. As was noted above, channels associated with “stiff” grains began to appear at ~670 MPa and as follows from the Figure, their number increased more or less smoothly. The contribution of TJP in channels formation looks like a jump at stress level of ~810-850 MPa.

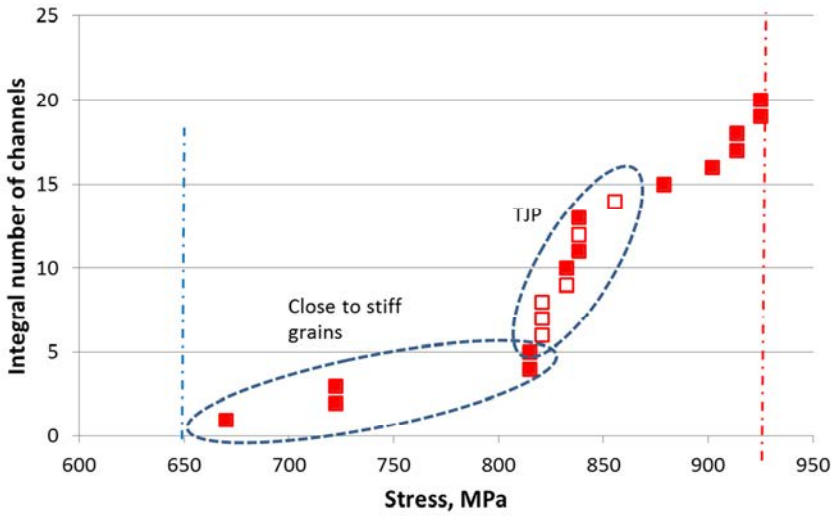

Fig. 27. Integral number of channels in the area investigated vs. calculated stress. Filled symbol – channel origin is related to stiff grain (>210 MPa), open symbol – channel started from triple junction point.

Many authors noted perfect spatial organization of the channels and their uniform spatial distribution; however, reasons leading to the formation of such ordered structure as a rule remained unexplored. It is interesting to investigate a dynamic picture of channels appearance and the evolution of the whole structure. It is especially important to find out is there any rule controlling the appearance of the following channels depending on existing ones. Such analysis was conducted for most grains shown in Fig. 26.

a) b)

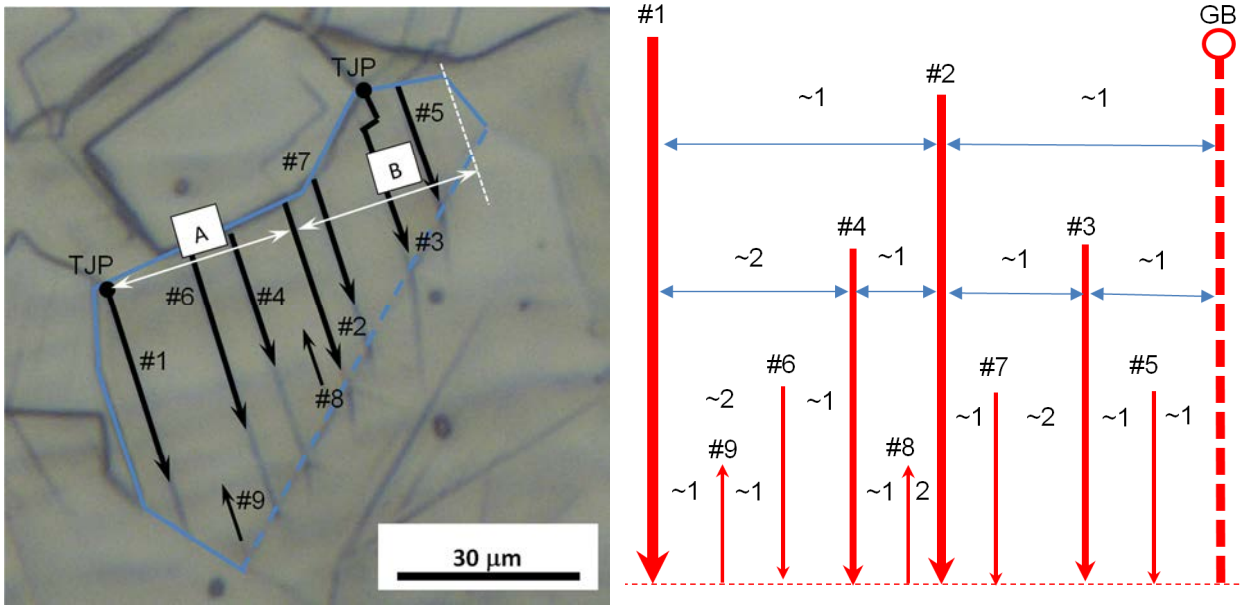

Fig. 28. Dislocation channels in a typical grain. a) Optic image, 600x. Arrows #1 – #9 show origin point and propagation direction of the channels. Thin solid lines show random grain boundaries, dash lines – twin boundary. b) Scheme.

.

Figure 28 shows the sequence of channels appearance in a typical grain. One can see that channel #1 formed at triple junction point which served as stress concentrator (this channel corresponds to #10 in Fig. 26). After that channel #2 appeared approximately at the middle between channel #1 and opposite grain boundary (A~B, see Fig. 28). All following channels formed at the middle or one third between existing channels of the previous generation (ratios ~1:1 or ~1:2; see scheme in Fig. 28). It is interesting that channel #3 appeared at TJP which location did not satisfy both 1:1 and 1:2 ratios, and because of that this channel demonstrated double turn and crossed the grain approximately at the middle between #2 and opposite grain boundary. Finally, two fine channels (#8 and #9 appeared from an opposite grain boundary, moved in back direction, but did not reach other grain boundary since deformation was stopped. These channels demonstrated ~1:2 and 1:1 ratios.

More fine channels, which were invisible for optic system, may exist in the grain, and it is not clear if they obey the spatial rule described above or not. Additional experiments with higher resolution are required. Since channels also have a height, and height should change along the channel length, the most promising way is in-situ experiments with the use of a laser confocal microscope.

Obviously, the shape of grain and its neighbors strongly influence an appearance of the spatial order and its degree. It was found that the phenomenon appeared most clear and was the most pronounced in elongated grains, which long axis was at 45 degree angle to the strain direction (see Fig. 28). Channels ordering phenomenon seems to be limited in the grains which long axis was parallel to the strain direction. At the same time, grain orientation is not a key parameter influencing the phenomenon; pronounced spatial organization was observed in different grains, and seemed not to be obstructed even in relatively hard and stiff [111] grains.

Also, spatial distribution rule is sensitive to the complexity of the grain shape; the more complex is grain shape (more TJP and internal twins) the less pronounced may be the spatial organization of channels. Figure 29 shows a complex shape grain with multiple internal twins (see Fig. 26 for detail). In this grain, channels #1, 2, 3, and 5 formed at stress concentrators like TJP and therefore do not obey the spatial distribution rule. Channel #4 appeared at ~1/3 between twin boundary and channel #1, however, the ratio is not perfect. Very interesting behavior was demonstrated by channel #6. This channel started at ~1/3 between channels #1 and #4 but later made a turn and followed to ~1/2 ratio.

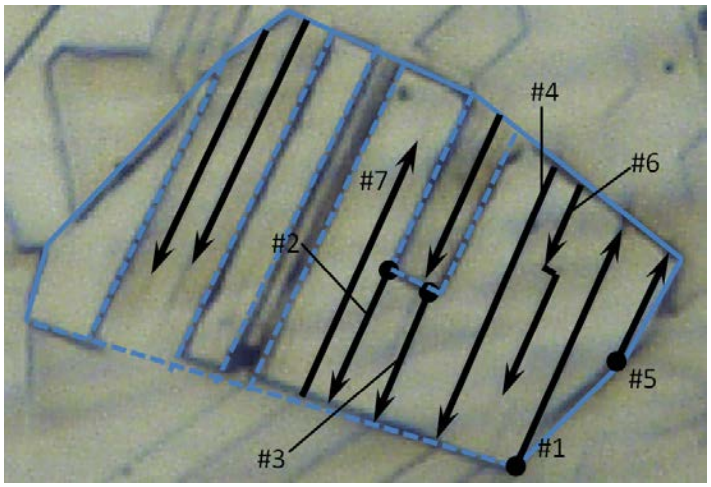

Fig. 29. Channels formation sequence in the grain of the complex shape. RHAB are shown by solid blue lines. RLAB and twin boundary are shown by dash lines. Black arrows indicate origin point and propagation direction of dislocation channels #1– #8, the numeration corresponds to the order of their appearance. Channels in annealing twins are not numerated.

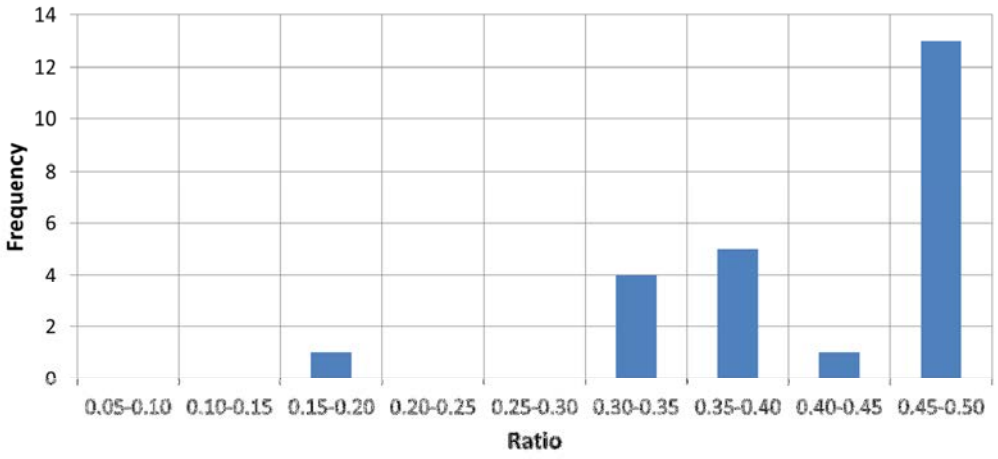

Fig. 30. Position of the next channel relative to existing ones (D/(A+B), where D=min(A,B), see Fig. 28).

Histogram in Figure 30 shows a position of the next channel relative to the channels of the previous generation; in the Figure, "0.5"-value means an exact middle position, "0.33" – position at one third between existing channels. In some cases, if channel appeared between an existing channel and grain boundary, the distances could not be measured properly; all such cases were excluded; in other words, Figure 30 represents only data related to interaction of channels. An exception was made for twin boundaries, which were parallel to the channel being measured. Also, it should be noted that in the case of the present work, the statistics were limited because of small strain level low channels density. Many grains contained just few (1 to 5) channels many of which were related to stress concentrators.

Nevertheless, data shown in Fig. 30 allows one to conclude that 1:1 and 1:2 ratios are most often observed. It is interesting that peak in the range of .35-0.40 does not correspond to exact 1:2 ratio (0.33...) and better agrees with "the golden ratio" (1:1.618 or ~0.38).

Most of the observed cases follow to the ratios noted above (1:1, 1:2, and probably 1:1.618); only few exceptions were found (see the point at the 0.15-0.20 range).

It is possible to expect that one of the driving forces of the phenomenon is back stress from dislocations pile-ups. Byun [10] discussed this aspect and offered a relationship which allows one to estimate back stress level at a potential origin point depending on distance from existing pile-ups. In the simplest case, according to [10] a minimum of the back stress level will be at the middle between two existing channels. So, the results listed in [10] allow one to explain the frequent appearance of new channel exactly between two existing ones. At the same time, the origin of the second spatial peak (~0.33) is not clear at the present.

3.3.4. Specific phase transformation associated with dislocation channeling

After bend experiment, the tensile strain level on the surface was 0.8% and SEM analysis found numerous channels formed on the surface; density of channels varied significantly from grain to grain. The average distance between channels visible at 600x (spacing) was 20-25 μm. Spacing value was relatively large because of the small strain, but it should decrease quickly if strain was increased. For instance, in [11] spacing was found to be ~4 μm at 3% strain and ~1.5 μm at 7%. The channels interacted with grain and twin boundaries that led to the change of their direction and height (see Fig. 31). At channel – grain boundary interaction points, dense populations of fine channels were often observed.

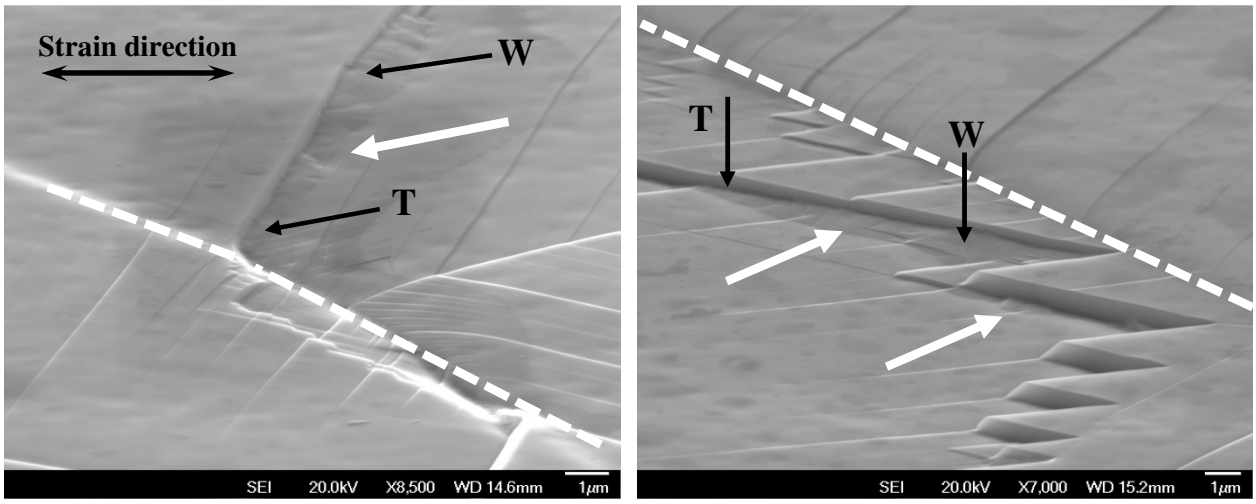

Fig. 31. Dislocation channels at the surface of deformed specimen. AISI 304 SS. 4.4 dpa, 0.8% strain. Hill-like structures are marked with white arrows. "T" and "W" symbols mark thin and wide portions of the "hills", respectively. White dash lines show grain boundaries.

However, in the case of the present work, such well-studied and expected deformation relief was accompanied with smooth hill-like (or ledge-like) structures. These formations had a width of ~1 micron and their height was ~25% of the channel height. The formations were observed only at the most developed channels. As a rule, they had elongated shapes (see Fig. 31) and in many cases started at grain boundaries. Often the width of the ledges varied along the length (compare positions marked as "W" and "T" in Fig.31). As discussed by Jiao *et al.* [8] and Edwards *et al.* [9], the interaction of the channel and grain boundary produces a heavily stressed region. Furthermore, any step at the surface causes a stress concentration and the larger the step the more volume that is affected by the increased local stress. Formation of ledges was observed only at high steps whose height exceeded ~150 nm. Therefore, one can assume the hill-like structures

form in localized regions of high stress and a potential critical volume with high stress is needed to cause the observed phenomena.

SEM-EBSD was employed to obtain crystallographic relationships and phase identification. In this case, an ability of phase identification was limited by high tilt angles. In some cases, channels shadowed the areas of interest. However, a number of EBSD patterns of high enough quality were obtained and indexed (see Fig. 32). As expected, areas lying close to channels maintained the austenitic (FCC) structure. However, the elongated hill-like formations along prominent dislocation channels (see Fig.31) were identified as having a BCC structure using EBSD (see Fig. 33) and believed to be deformation martensite. Each hill formation consisted of a colony of BCC-grains with an average grain size of 0.5-2 μm. As a rule, the area around a single BCC-grain had very low image quality index (IQ), although the IQ index was high enough for phase identification within the BCC-grain. Low local IQ value can be explained by high local stresses and strains around BCC-grains. Martensitic transformation in austenitic steels often has complex character (FCC→HCP→BCC, where HCP is hexagonal close packed or ε-martensite [12]); however, in the present work no evidence of HCP-phase was observed.

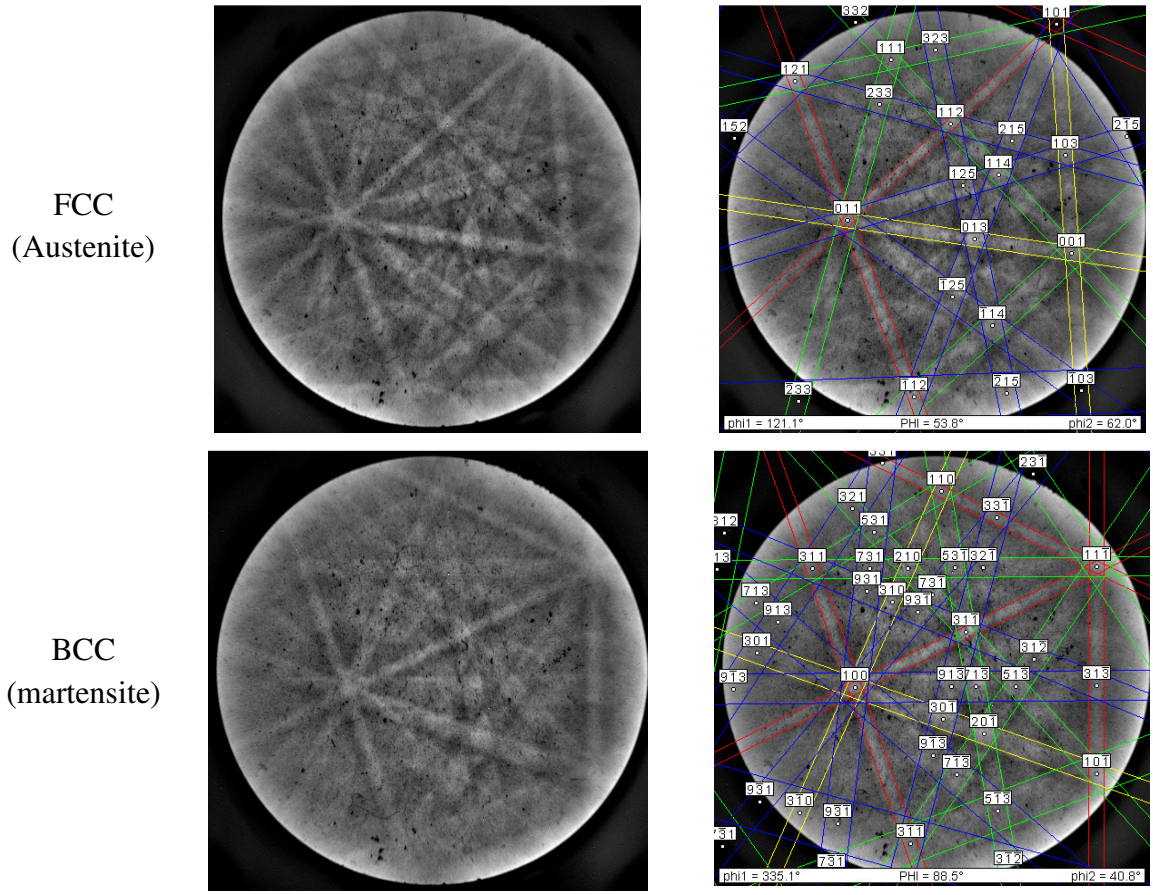

Fig. 32. Typical non-indexed (left) and indexed (right) patterns of FCC and BCC phases.

Most of the BCC-grains in a single hill had the same crystallographic orientation; a small fraction (~10% or below) had a different orientation. As was noted in [13], from a theory point of view up to 24 orientation variants of BCC-phase are possible during the FCC-to-BCC martensitic transformation. These variants are equally probable during isothermal transformation; however, during plastic deformation strong variants selection exists [14] and usually only 3-4 martensite orientation variants are observed. In the present work, not more than two variants were observed in the transformed area along the channel. Always one of the variants was dominating. It allows one to conclude that variant selection during martensite formation at dislocation channels on a free surface is stronger than during plastic flow of unirradiated steels.

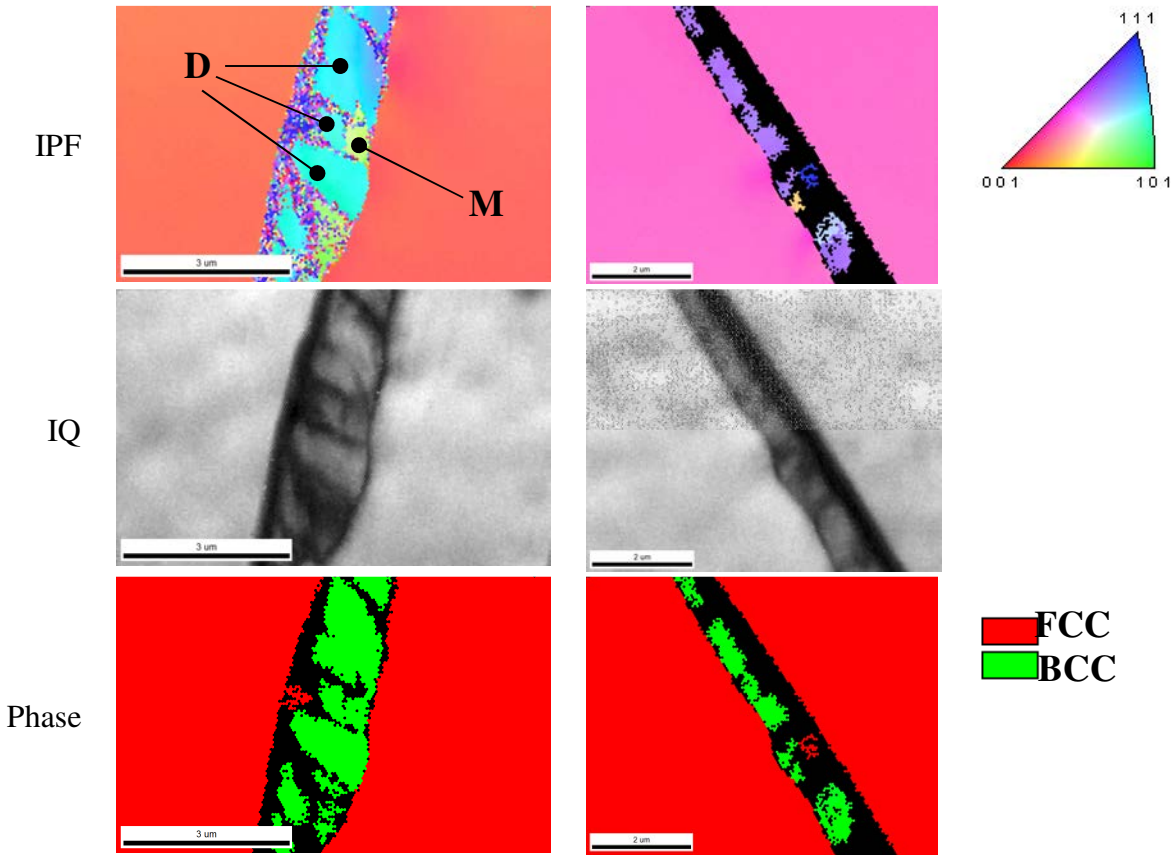

Fig. 33. EBSD maps (IPF, IQ, and phase) for channels with martensitic hills. Points with low confidence index (<0.1) which are indicated with black pixels in the right IPF image and small grains (<20 pixels) were excluded from the analysis. Symbol "D" marks martensitic grain with the dominant orientation; "M" shows grain with the second (minor) orientation.

Based on EBSD results, average martensite amount in the near-surface layer can be estimated by ~0.4-0.8%. Ferroprobe is not a surface-sensitive analysis technique; therefore one can conclude that all martensite is localized in very thin (few microns maximum) layer.

Martensite amount varied significantly from grain to grain depending on grain orientation to the straining direction. Figure 34 shows the influence of grain orientation on martensite formation at dislocation channels. As follows from the Figure, martensite may form at a dislocation channel if grain orientation is close to the [001]-[111] line, as well as the mentioned channel height exceeding ~150 nm. No martensite formation was observed at channels in [101] grains even at step heights of 200-300 nm or above. It is possible to conclude that grain orientation is one of key parameters influencing the phenomenon. At the same time, as follows from the results, grains with the same orientation may or may not have this specific form of martensite.

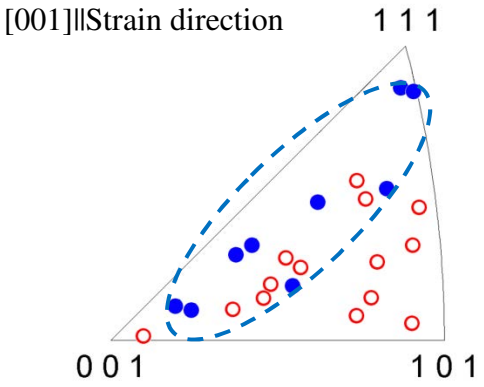

Fig. 34. Orientation of grains with (filled circles) and without (open circles) martensite at dislocation channels. Channels in the grains presented in the figure have comparable height (~150 nm or above). Finer channels were omitted since no martensite was observed at the fine channels regardless grain orientation.

So, in the present section, surface relief and localized deformation in 4.4-dpa irradiated AISI 304 stainless steel were investigated using scanning microscopy and electron backscattering diffraction. It was found that BCC-phase (deformation martensite) had formed at the surface of the deformed specimen along specific dislocation channels. Martensitic hill-like formations had widths of ~1 μm and depths of ~3-4 μm and were observed at channels with height of ~0.15 μm or above. This specific martensite associated with dislocation channels was observed in grains oriented along [001]-[111] line but not in [101]-grains.

4. Conclusions and future plans

To overcome limitations caused by irradiated materials availability, new miniature bend test assembly was designed and produced. The assembly allows one to conduct 3- and 4-point bend tests with various span distances and provides an ability to conduct in-situ optic measurements and microstructure observations. A set of materials including 304 and 316 stainless steels and model alloys irradiated up to 47 dpa was tested using the assembly. Bend test method coupled with finite element modeling allows one to define mechanical properties of material, investigate

its deformation behavior, and define stress and strain distribution in the deformed specimen which is important for further structure investigation.

Using specimens subjected to bend test, deformation modes were studied for a set of irradiated austenitic steels and alloys. Phase and structure transformations (martensite formation and twinning, respectively) were investigated in 304 stainless steel and Si-depleted model E-alloy. New results on morphology of twins and martensite in irradiated materials were obtained. Dynamics of deformation localization and dislocation channeling was studied in-situ. Some interesting data on dislocation channels evolutions were obtained and are analyzing; one of the interesting results is channels spatial organization. Also, specific new form of deformation martensite associated with dislocation channels was firstly found and analyzed.

Future work will include additional deformation experiments at different strain rate and/or test temperature, also as more detailed channels dynamics investigation using SEM-EBSD and laser confocal microscope. Also, it is planned to expand finite element analysis method to a meso-scale level and investigate a group of interacting grains; it is important to investigate stress and strain distribution and understand a driving force of early channels formation. Some efforts will be done on understanding phase and structure transformations and on establishing material instability parameter which controls twinning and martensite formation. If this is done, phase instability and deformation modes may be evaluated and managed during long-term irradiation.

5. References

1. Scott, Materials Reliability Program: A Review of the Cooperative Irradiation Assisted Stress Corrosion Cracking Research Program (MRP-98), EPRI Report 1002807, 2003.
2. J. P. Massoud, P. Dubuisson, P. Scott, and V. K. Chamardine, CIR II Program: Description of the Boris 6 and 7 Experiments in the BOR-60 Fast Breeder Reactor, EPRI Report 1011787, 2005.
3. K. Suzuki, S. Jitsukawa, N. Okubo, F. Takada, J.Nucl.Eng. and Design 240 (2010) 1290–1305.
4. B. Pan, K. Qian, H. Xie, A. Asundi, Measurement Science and Technology, 20 (2009) 1–17.
5. Stuart A. Maloy, A. Zubelewicz, T. Romero, M.R. James, W.F. Sommer, Y. Dai, J. Nucl. Mater.343 (2005) 191–196.
6. Gussev M.N., T.S. Byun, J.T. Busby, J. Nucl. Mater. 427 (2012) 62-68.
7. G.S. Was, Y. Ashida, P.L. Andresen, Corrosion Review 29 (2011) 7–49.
8. Z. Jiao, G.S. Was, J. Nucl. Mater. 408 (2011) 246–256.
9. D.J. Edwards, B.N. Singh, J. Nucl. Mater. 329–333 (2004) 1072–1077.
10. T.S.Byun, N.Hashimoto, J. Nucl. Mater. 354 (2006) 123-130.
11. Z. Jiao, J. T. Busby, R. Obata, G. S. Was, Influence of Localized Deformation on Irradiation-assisted Stress Corrosion Cracking of Proton-irradiated Austenitic Alloys Proceedings of the 12th International Conference on Environmental Degradation of Materials in Nuclear Power

System – Water Reactors – *Edited by T.R. Allen, P.J. King, and L. Nelson TMS (The Minerals, Metals & Materials Society), 2005, 379–387.*
12. A. Das, S. Tarafder, Int. J. Plast. 25 (2009) 2222–2247.
13. B. Petit, N. Gey, M. Cherkaoui, B. Bolle, M. Humbert, Int. J. Plast. 23 (2007) 323–341.
14. D. Marechal, L. Malet, S. Godet, C. Sinclair1, Materials Science Forum 702-703 (2012) 850–853.